ADER scheme for incompressible Navier-Stokes equations on Overset grids with a compact transmission condition

Michel Bergmann, Michele Giuliano Carlino, Angelo Iollo, Haysam Telib

HAL Id: hal-03263417
https://hal.inria.fr/hal-03263417

Submitted on 17 Jun 2021

ADER scheme for incompressible Navier-Stokes equations on overset grids with a compact transmission condition

Michel Bergmann, Michele Giuliano Carlino, Angelo Iollo, Haysam Telib

ADER scheme for incompressible Navier-Stokes equations on overset grids with a compact transmission condition

Michel Bergmann[*][†], Michele Giuliano Carlino[*][†][‡], Angelo Iollo[*][†], Haysam Telib[§]

Project-Team MEMPHIS

Abstract: A space-time Finite Volume method is devised to simulate incompressible viscous flows in an evolving domain. Inspired by the ADER method, the Navier-Stokes equations are discretized onto a space-time overset grid which is able to take into account both the shape of a possibly moving object and the evolution of the domain. A compact transmission condition is employed in order to mutually exchange information from one mesh to the other. The resulting method is second order accurate in space and time for both velocity and pressure. The accuracy and efficiency of the method are tested through reference simulations.

Key-words: Chimera mesh; Overset grid; ADER; Finite Volume; incompressible Navier-Stokes; compact transmission condition

Email: michel.bergmann@inria.fr, michele-giuliano.carlino@inria.fr, angelo.iollo@inria.fr, haysam.telib@optimad.it

[*] INRIA Bordeaux Sud-Ouest, MEMPHIS team, 200 avenue de la vielle tour, 33405 Talance, France
[†] IMB, Institut de Mathématiques de Bordeaux, 351 cours de la Libération, 33405 Talance, France
[‡] Corrensponding author
[§] Optimad Engineering srl, via Agostino da Montefeltro 2, 10134 Turin, Italy

Schéma ADER pour les équations incompressibles de Navier-Stokes sur des maillages overset avec une condition de transmission compacte

Résumé :   Une méthode des volumes finis spatio-temporels est conçue pour simuler des écoulements visqueux incompressibles dans un domaine évolutif. Inspirée de la méthode ADER, les équations de Navier-Stokes sont discrétisées sur un maillage spatio-temporel overset qui est capable de prendre en compte à la fois la forme d'un objet éventuellement en mouvement et l'évolution du domaine. Une condition de transmission compacte est employée afin d'échanger mutuellement des informations d'un maillage à l'autre. La méthode résultante est d'une précision de second ordre dans l'espace et dans le temps pour la vitesse et la pression. La précision et l'efficacité de la méthode sont testées sur des cas test pris de la littérature.

Mots-clés :   Maillage Chimera; Maillage overset; ADER; Volumes Finis; Navier-Stokes incompressible; condition de transmission compacte

Contents

1 Introduction

The simulation of flows in complex unsteady geometries such as fluid-structure interaction, freely moving objects or moving boundaries induced by the flow itself requires specific numerical modelling. It is possible to distinguish three main classes of methods for these flow phenomena: the Arbitrary Lagrangian-Eulerian (ALE) methods, interface methods and Chimera meshes approaches. The ALE methods [1, 2] are accurate and allow a sophisticate grid displacement and mesh adaptation after a proper reformulation of the governing equations. However, when the grid deformation is affected by an excessive stretch, a computationally expansive remeshing may be necessary. Consequently, further numerical errors deriving from the interpolation of data from the old grid to the new mesh need to be managed. In interface methods, such as Ghost boundary methods [3], immersed boundary methods [4] and penalization methods [5], the physical domain is discretized through a simple mesh, usually structured and Cartesian, not changing in time [6, 7]. For this reason, the mesh does not necessary fit the moving boundary and a special care has to be taken to attain a sufficient degree of accuracy at the physical boundaries. Moreover, because of the simplicity of the mesh and its unique aspect ratio, the presence of thin boundary layers could significantly affect the computational advantages of these methods. Hybrid techniques employing immersed boundary methods with anistropic mesh adaptations can be employed for circumventing this problem [8].

    Our investigations focus on Chimera grids [9, 10, 11, 12]. They consist of multiple overlapping mesh blocks that together define an overset grid. Usually, one has a background mesh that includes one or more foreground mesh patches that are fitted to the physical domain boundaries. This mesh generation strategy considerably simplifies the task of mesh adaptation in the case of boundary layers, changing geometry for an unsteady problem and for unsteady multiply connected domains. Once the multiple mesh patches are generated, they are collated in order to obtain an appropriate overlapping zone between the neighboring

blocks [11]. In the overlapping zones, the exchange of solution information from one grid to another is performed. A compact transmission condition is generally sought in order to limit communications between the grids. However, when a minimal number of cells are locally employed for transferring information among the computational blocks, the order of the scheme can be degraded.

Generally, the numerical solution on Chimera grids is obtained in two steps. In a first step one computes the solution in the background mesh and in a second step in the foreground mesh by strongly imposing at the boundaries of the latter mesh the solution found in the previous step. For example, in [13, 14, 15], fringe (namely *donor*) cells of a block in proximity of the overlapping zone provide the information to the fringe (i.e., *receptor*) cells of another block by polynomial interpolation. This oneway approach from the background to the foreground mesh through *donor/receptor* cells was originally proposed in [16]. Another way of making the different blocks communicate is to use proper Domain Decomposition (DD) methods (e.g., Schwartz, Dirichlet/Neumann or Dirichlet/Robin methods). In particular, each mesh block is considered as a decomposition of the domain and the overlapping zones are the interfaces for coupling the different blocks. Accordingly to these approaches, typically iterative discrete methods are employed. For this two way communication, the reader is referred to [17] for further details.

In this paper, we propose a space-time Finite Volume (FV) scheme on Chimera grids. Our objective is to combine some aspects of an ALE approach, notably its flexibility with respect to grid displacement and deformation, to the multi-block discretization strategy of overset grids. In particular, special care is devoted to grid overlapping zones in order to devise a compact and accurate discertization stencil to exchange information between different mesh patches. The numerical solution of the incompressible Navier-Stokes equations follows a classical fractional method [18, 19] with a second-order accuracy in space and time.

The Arbitrary high order DERivatives (ADER) method provides an ideal setting for the resolution of the nonlinear unsteady convection-diffusion equation with a moving grid. In [20, 21, 22, 23], the authors present a method to recover an accurate solution for hyperbolic differential problems with an arbitrary order of accuracy on a single mesh block. The numerical scheme treats the temporal variable indistinctly with respect to the spatial variables by defining the solution on a space-time slab. This discretization approach, therefore, allows us to re-consider the problem of Chimera grids transmission conditions. Instead of time-dependent spatial transmission conditions between relatively moving grid blocks, we define interpolation polynomials on arbitrarily intersecting space-time cells at the block boundaries. In the ADER scheme a local space-time weak solution of the problem from the generic time t to $t + \Delta t$ is computed in every single space-time cell. This solution is defined as the *predictor*. The prediction step is local and hence embarrassingly parallel, because the solution is calculated independently of the information of the neighbouring cells. Then, in the subsequent stage of *correction*, the computation of a space-time numerical flux between neighboring cells provides the appropriate stabilization of the integration scheme. We extend this method for the incompressible Navier-Stokes equations on overset grids, in the spirit of our previous work [24].

For the resolution of the Poisson equation in the projection step, we propose a hybrid FV method. On internal cells, a classical reconstruction of the gradient through the diamond formula [25, 26] is employed. On fringe cells, inspired by [27], the reconstruction of the gradient is performed by interpolating the data through an appropriate local minimization taking into account the geometry of the stencil. Special care is devoted to the definition of a fully conservative scheme in the limit of a no-shift overlapping configuration, namely when the background and foreground meshes coincide in the overlapping region.

2   The overset grid

An overset grid or Chimera mesh is a set of mesh blocks covering the computational domain. Each block may overlap other block(s) in some particular sub-region(s) said *overlapping zone(s)*. Once the multiple mesh patches are generated, they are collated in order to have an appropriate topology [11]. In the sequel, the method is explained by considering a two block overset grid (i.e., the background and the foreground meshes). Figure 1 shows an overset grid composed by one background mesh (in black) surrounding one foreground mesh (in blue). In many situations, the foreground mesh can move and deform. The overlapping zone is necessary for the communication and data transfer from one mesh to the other.

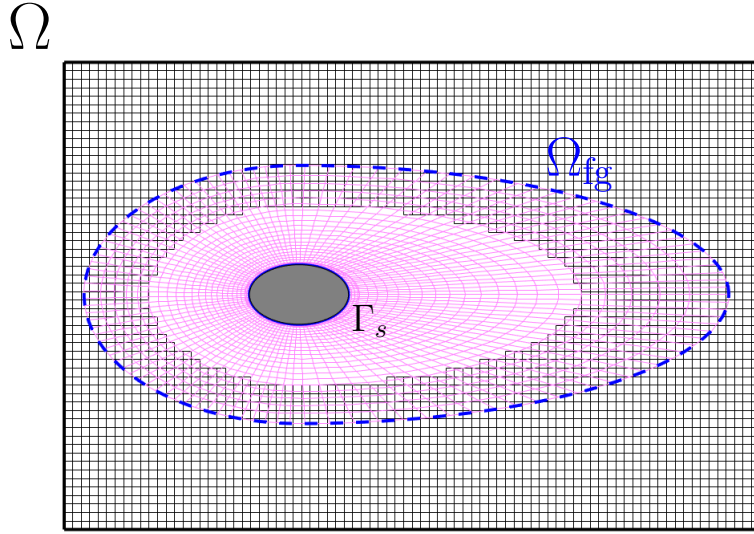The computational cell of any block mesh is quadrilateral in this work.

Figure 1: Sketch of the mesh configuration. The computational (i.e. fluid) domain contains the solid body whose boundary is Γ_s. The foreground mesh (in blue) defines the foreground subdomain Ω_{fg} whose boundary is the union of an external (dashed line) and internal (continuous line) boundary. Consequently, the internal foreground boundary coincides with the solid body boundary.

2.1 Automatic definition of the stencil and transmission condition

Let $\mathcal{T}_k = \{\Omega_i^k\}_{i=1}^{N_k}$ be the partition composed of N_k cells referring to the k-th block mesh. In order to simplify the notation, in the following we will omit the superscript k to the cell Ω_i^k by writing Ω_i. Let $\mathcal{S}_i$ the stencil centered over the cell Ω_i. Thus, stencil $\mathcal{S}_i$ is the set collecting the indexes of neighboring cells to Ω_i. By abuse of language, sometimes we will refer to the physical set $\Omega_i \cup \bigcup_{j \in \mathcal{S}_i} \Omega_j$ as the stencil.

It is possible to distinguish two classes of cells with respect to their proximity to the overlapping interface. The definition of the stencil depends on the class it belongs to.

If cell Ω_i is not at the boundary of the overlapping zone (Figure 2a), the stencil $\mathcal{S}_i$ is composed of all the cells Ω_j sharing at least one vertex with Ω_i. Thus, if Ω_i belongs to the partition $\mathcal{T}_1$, all cells Ω_j, with $j \in \mathcal{S}_i$, also belong to $\mathcal{T}_1$.

If the cell Ω_i of partition $\mathcal{T}_k$ is at the boundary of the interface, it is no longer possible to use the criterion of the cells sharing at least a vertex. In fact, there will be at least one edge e_{il} not shared by any other cell of the same partition (see right edge of cell Ω_{16} in Figure 2b). For these cells, we systematically identify other cells of partition $\mathcal{T}_j$ ($j \neq k$) belonging to the stencil. Let the extremes of the edge be indicated as $\boldsymbol{v}_1$ and $\boldsymbol{v}_2$ and its middle point with $\boldsymbol{v}_3$, respectively. Point $\boldsymbol{c}_\star$ is the center of mass of generic cell $\Omega_\star$. For our numerical tests, Algorithm 1 is adopted through the two steps:

1. look for the nodes of cells of the other partition $\mathcal{T}_j$ minimizing the Euclidean distance with respect to points $\boldsymbol{v}_\mu$, $\mu = 1, 2, 3$, (line 5, see Figure 3a);

2. compute the symmetric points $\tilde{\boldsymbol{v}}_\mu$ of center $\boldsymbol{c}_i^k$ with respect to points $\boldsymbol{v}_\mu$ for $\mu = 1, 2, 3$ (line 6), then look for the cells of partition $\mathcal{T}_j$ whose centers minimize the Euclidean distance with the three symmetric points (line 7, see Figure 3b).

For the edges shared by other cells in the same partition, the cells of the stencil will be those ones sharing at least one vertex (as cells of indexes 13, 14, 17, 19 and 20 in Figure 2b).

The routine presented in this section will be run whenever the foreground mesh configuration as well as the hole change.


Algorithm 1 Compute stencil for cells at the boundary of the overlapping zone.

Require: $\Omega_i^k, e_{il}^k, \mathcal{T}_j, \mathcal{S}_i^k$;   ▷ $j \neq k$, i.e. $\mathcal{T}_j$ is the other partition with respect to $\mathcal{T}_k$
 1: Initialize $\boldsymbol{v}_1$ and $\boldsymbol{v}_2$ as the two vertexes of edge e_{il}^k;
 2: $\boldsymbol{v}_3 \leftarrow (\boldsymbol{v}_1 + \boldsymbol{v}_2)/2$;   ▷ Middle point of edge e_{il}^k
 3: $\mathcal{Z}_j \leftarrow \emptyset$;   ▷ Temporary set of indexes of partition $\mathcal{T}_j$
 4: **for** $\mu = 1, 2, 3$ **do**
 5:     $\mathcal{Z}_j \leftarrow \mathcal{Z}_j \cup \{n = 1, \ldots, N_j : \|\boldsymbol{v}_\mu - \boldsymbol{c}_n^j\| \leq \|\boldsymbol{v}_\mu - \boldsymbol{c}_m^j\| \quad \forall m = 1, \ldots, N_j\}$;
 6:     $\tilde{\boldsymbol{v}} \leftarrow 2\boldsymbol{v}_\mu - \boldsymbol{c}_i^k$;   ▷ Symmetric point of cell-center $\boldsymbol{c}_i^k$ of Ω_i^k with respect to $\boldsymbol{v}_\mu$
 7:     $\mathcal{Z}_j \leftarrow \mathcal{Z}_j \cup \{n = 1, \ldots, N_j : \|\tilde{\boldsymbol{v}} - \boldsymbol{c}_n^j\| \leq \|\tilde{\boldsymbol{v}} - \boldsymbol{c}_m^j\| \quad \forall m = 1, \ldots, N_j\}$;
 8: $\mathcal{S}_i^k \leftarrow \mathcal{S}_i^k \cup \mathcal{Z}_j$;
 9: **return** $\mathcal{S}_i^k$
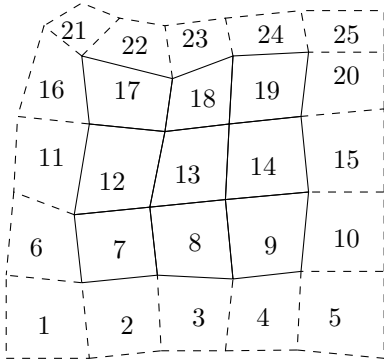
(a) A stencil of cells in the same partition.   Continuous line for the stencil $\mathcal{S}_{13} = \{7, 8, 9, 12, 14, 17, 18, 19\}$.
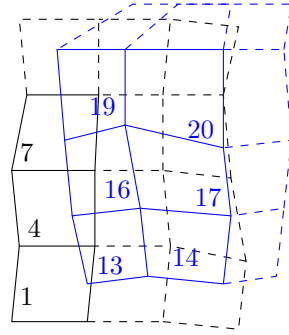
(b) A stencil of cells not belonging to the same partition. Continuous line for the stencil $\mathcal{S}_{16} = \{1, 4, 7, 13, 14, 17, 19, 20\}$.

Figure 2: Two possible stencils: on the right the stencil is in the same partition; on the left the stencil is composed of cells not belonging to the same partition.

3   The governing equations

Let $\Omega(t) \subset \mathbb{R}^2$ be the computational domain, eventually evolving in time $t \in [0, T]$, with T positive real. We aim in studying the two-dimensional incompressible flow in the space-time domain $\Omega(t) \times (0, T)$ governed by the system

$$\rho\left(\frac{\partial \boldsymbol{u}}{\partial t} + (\boldsymbol{u} \cdot \nabla)\boldsymbol{u}\right) = -\nabla p + \mu \Delta \boldsymbol{u} \qquad \text{in } \Omega(t) \times (0, T), \tag{1a}$$

$$\nabla \cdot \boldsymbol{u} = 0 \qquad \text{in } \Omega(t) \times (0, T), \tag{1b}$$

$$\boldsymbol{u}(\boldsymbol{x}, 0) = \boldsymbol{u}_0(\boldsymbol{x}) \qquad \text{in } \Omega(0) \times \{0\}, \tag{1c}$$

and completed with boundary conditions over $\partial\Omega(t) \times (0, T)$. In system (1), the unknowns are the velocity $\boldsymbol{u}$ and the pressure p of the fluid of density ρ and dynamic viscosity μ. The initial condition is given by (1c) through the initial velocity $\boldsymbol{u}_0$. Sometimes, it is more convenient to study the nondimensionalized system of (1); in this case, through the incompressibility condition (1b), equations (1a) become

$$\frac{\partial \boldsymbol{u}}{\partial t} + \nabla \cdot (\boldsymbol{u}\boldsymbol{u}^T) = -\nabla p + \frac{1}{\text{Re}}\Delta \boldsymbol{u} \quad \text{in } \Omega(t) \times (0, T), \tag{2}$$

where $\text{Re} = \rho u_\infty L/\mu$ is the Reynolds number, with u_∞ the characteristic velocity of the fluid and L the characteristic length of either the physical domain or the obstacle, if it is present.

The domain $\Omega(t)$ is discretized with an overset mesh whose background and foreground partitions are $\mathcal{T}_{\text{bg}}$ and $\mathcal{T}_{\text{fg}}$, respectively. For the sake of simplicity we consider only one foreground mesh even though it is possible
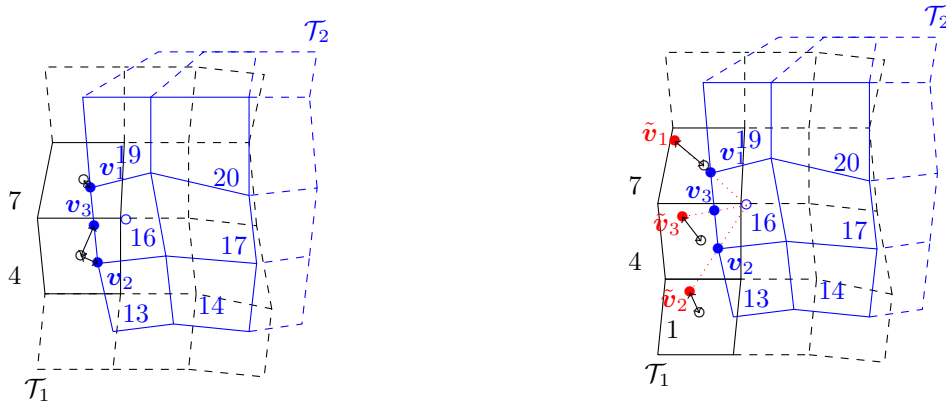
(a) First step: by identifying the vertexes $\boldsymbol{v}_1$ and $\boldsymbol{v}_2$ and the middle point $\boldsymbol{v}_3$ of the edge on the boundary cell Ω_{16} (blue full dots), look for the nodes of cells in the partition $\mathcal{T}_1$ (black empty dots) minimizing the Euclidean distance with respect to those points.

(b) Second step: by identifying the symmetric points $\tilde{\boldsymbol{v}}_\mu$, $\mu = 1, 2, 3$, (red full dots) of the node of the cell Ω_{16} (blue empty dot) with respect to the vertexes and the middle point of the non-shared edge, look for the nodes of cells in the partition $\mathcal{T}_1$ minimizing the Euclidean distance to those points.

Figure 3: The two steps for the research of cells in the partition $\mathcal{T}_1$ for the cell $\Omega_{16} \in \mathcal{T}_2$.

to extend the method by employing several foreground meshes. The cells of the foreground partition define a subset Ω_{fg} of the physical domain. The foreground mesh of coordinates $\boldsymbol{X}$ are allowed to move and deform accordingly to the motion equation

$$\frac{\mathrm{d}\boldsymbol{X}}{\mathrm{d}t} = \boldsymbol{V} \quad \text{in } (0, T), \tag{3}$$

which is a Cauchy problem of initial condition $\boldsymbol{X}|_{t=0} = \boldsymbol{X}_0(\boldsymbol{x})$. In problem (3) the force term is the mesh velocity $\boldsymbol{V}(\boldsymbol{x}, t; \boldsymbol{u}, p)$, eventually dependent on the fluid velocity and pressure (in that case systems (1) and (3) are coupled). The motion equation (3) can be imposed regardless of the physics described by system (1). However, when studying fluid-structure interaction phenomena, the foreground mesh is employed in order to easily take into account the generic shape of the solid body. Consequently, the computational domain $\Omega(t)$ defines the fluid domain and part of the boundary of the foreground subdomain Ω_{fg} discretizes the boundary Γ_s of the solid, i.e., $\Gamma_s \subset \partial\Omega_{\mathrm{fg}}$ (see Figure 1). Along the boundary Γ_s the interaction between the fluid and the solid takes place and it mathematically reads

$$\boldsymbol{u} = \boldsymbol{u}_B \quad \text{on } \Gamma_s(t) \times (0, T), \tag{4}$$

where $\boldsymbol{u}_B$ is the velocity of the solid body. Thus, the mesh velocity $\boldsymbol{V}$ has to coincide with the velocity $\boldsymbol{u}_B$ of the body on the boundary Γ_s of the solid:

$$\boldsymbol{V}\big|_{\Gamma_s} \equiv \boldsymbol{u}_B. \tag{5}$$

Consequently, the dynamics of motion and deformation of the foreground mesh in (3) is led by condition (5).

4 The numerical method

The Navier-Stokes equations (1) are discretized using a Finite Volume (FV) scheme with the collocated cell-centered variables $(\boldsymbol{u}, p)$. Let the whole time interval $(0, T)$ be subdivided into N sub-intervals (t^n, t^{n+1}), $n = 1, \ldots, N - 1$, of length Δt. For a given variable $\phi(\boldsymbol{x}, t)$, we indicate its evaluation at discrete time t^n with ϕ^n. A fractional step method is used to evaluate the solution in time. In order to improve the pressure smoothness and avoid some odd-even oscillation phenomena, the face-centered velocity

$$\boldsymbol{U} = (\boldsymbol{u})_{\mathrm{fc}} \tag{6}$$

is introduced as presented by Mittal *et al.* [28]. The symbol $(\cdot)_{\text{fc}}$ is a discrete operator computing the face-centered value of the cell-centered input and it will be explained at the end of this section.

Based on the predictor-projection-correction non incremental Chorin-Temam scheme [18, 19], the first step (predictor step) evaluates an intermediate velocity $\boldsymbol{u}^*$ obtained by the resolution of an unsteady convection-diffusion equation

$$\begin{cases} \frac{\partial \boldsymbol{u}^*}{\partial t} + \nabla \cdot \left(\boldsymbol{u}^*(\boldsymbol{U}^n)^T\right) - \frac{1}{\text{Re}}\Delta \boldsymbol{u}^* = \boldsymbol{0} & \text{in } \Omega(t) \times (t^n, t^{n+1}) \\ \boldsymbol{u}^* = \boldsymbol{u}^n & \text{in } \Omega^n \times \{t^n\} \end{cases}, \tag{7}$$

which will be numerically solved as explained in the next subsection.

The intermediate velocity $\boldsymbol{u}^*$ solving problem (7) is not divergence free. Thus the predicted field $\boldsymbol{u}^*$ is projected onto a divergence free space through the pressure. As a matter of fact, by computing the divergence of equation

$$\frac{\boldsymbol{u}^{n+1} - \boldsymbol{u}^*}{\Delta t} = -\nabla p^{n+1} \quad \text{in } \Omega(t) \times (t^n, t^{n+1}) \tag{8}$$

and applying the divergence condition (1b) on the velocity fluid $\boldsymbol{u}^{n+1}$, we obtain the Poisson equation for the pressure

$$\Delta \psi^{n+1} = -\nabla \cdot \boldsymbol{u}^* \quad \text{in } \Omega^{n+1}, \tag{9}$$

with $\psi = \Delta t\, p$, by defining the projection step. Problem (9) refers to the cell-centered velocity field and pressure. Thus, by employing the face-centered intermediate velocity $\boldsymbol{U}^* = (\boldsymbol{u}^*)_{\text{fc}}$, problem (9) turns into

$$\Delta \psi^{n+1} = -\nabla \cdot \boldsymbol{U}^* \quad \text{in } \Omega^{n+1}, \tag{10}$$

which is numerically solved as explained in Section 4.2.

The velocity fields $\boldsymbol{u}^{n+1}$ and $\boldsymbol{U}^{n+1}$ at the cell-centers and face-centers, respectively, are finally corrected through equation (8) as

$$\boldsymbol{u}^{n+1} = \boldsymbol{u}^* - \nabla \psi^{n+1}, \tag{11a}$$

$$\boldsymbol{U}^{n+1} = \boldsymbol{U}^* - (\nabla \psi^{n+1})_{\text{fc}}, \tag{11b}$$

which conclude the numerical routine within the time sub-interval from t^n to t^{n+1}.

4.1 The predictor solution

In this subsection the numerical scheme for the predictor equation (7) solved by the intermediate velocity $\boldsymbol{u}^*$ is presented. The method consists in a FV predictor-corrector scheme stabilised with a Local Lax-Friedrichs approach. It was originally presented in our previous work [24] for a generic advection-diffusion (eventually nonlinear) problem where the computational domain is discretized by employing overset grids. It is inspired by the ADER (Arbitrary high-order DERivatives) method [20, 21, 22, 23] and was reformulated for both the presence of the diffusion and the management of the dynamics for the Chimera mesh.

4.1.1 Local space-time Galerkin predictor and foreground mesh motion

The first step of the method for the unsteady convective-diffusive equation (7) consists in the research of a weak solution in any cell of the mesh. Let $\mathcal{C}_i^n = \Omega_i(t) \times (t^n, t^{n+1})$ be the physical space-time cell whose lower and upper bases represent the evolution of the i-th cell $\Omega_i(t)$ from time t^n to t^{n+1}. Problem (7) is rewritten with respect to a space-time reference system identified by the independent variables $\boldsymbol{\xi} \equiv (\xi, \eta, \tau)$ in the unit cube $\hat{\mathcal{C}} = (0, 1)^3$. As originally proposed in [29], it is discretized through a nodal formulation of space-time nodes given by a tensor product of three Gauss-Legendre quadrature points along space and time directions. This choice defines an $L^2(\hat{\mathcal{C}})$-orthogonal Lagrange basis used for the approximation of the Galerkin solution. Consequently, over a space-time cell there are 27 Gauss-Legendre nodes $\hat{\boldsymbol{\xi}}_m$ and 27 Lagrange polynomials $\theta_l : \hat{\mathcal{C}} \to \mathbb{R}$ such that

$$\theta_l(\hat{\boldsymbol{\xi}}_m) = \delta_{lm} \quad \text{and} \quad \int_{\hat{\mathcal{C}}} \theta_l \theta_m \, \mathrm{d}\boldsymbol{\xi} = \delta_{lm}, \quad l, m = 1, \dots, 27,$$
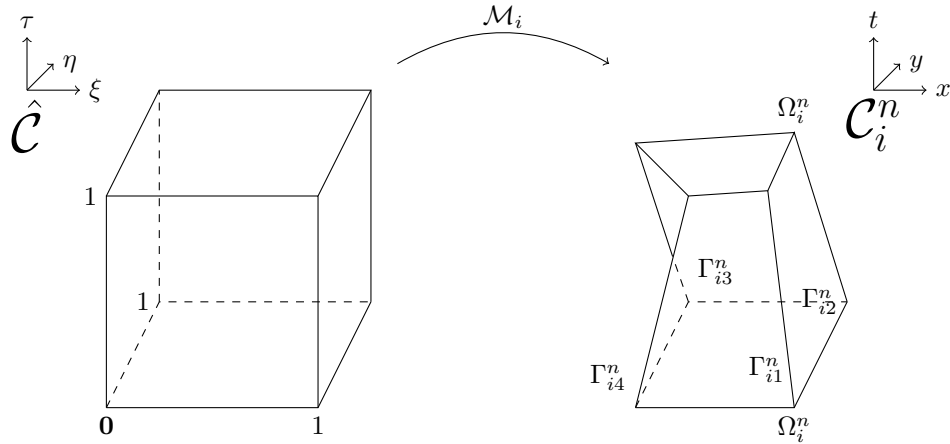
Figure 4: Sketch of the map $\mathcal{M}_i$ from the reference space-time cell $\hat{\mathcal{C}}$ to the physical space-time cell $\mathcal{C}_i^n$. The boundary $\partial \mathcal{C}_i^n$ of the physical space-time cell is defined by the spatial cells Ω_i^n (lower base) and Ω_i^{n+1} (upper base) and by the space-time boundaries Γ_{ij}^n, $j = 1, \ldots, 4$, linking any edge of Ω_i^n to any edge of Ω_i^{n+1}.

where δ_{lm} is the Kronecher symbol.

The component-wise problem to be solved is: *find $q_k : \mathcal{C}_i^n \to \mathbb{R}$, $k = 1, 2$, such that*

$$\begin{cases} \partial_t q_k + \nabla \cdot \boldsymbol{F}(q_k, \nabla q_k) = 0 & \text{in } \mathcal{C}_i^n \\ q_k = \Pi_i u_k^n & \text{on } \Omega_i^n \end{cases}, \tag{12}$$

where $\boldsymbol{F}(q_k, \nabla q_k) = \boldsymbol{q} q_k - \nabla q_k / \text{Re}$ is the convective-diffusive term. Problem (12) is problem (7) restricted to the physical space time-cell $\mathcal{C}_i^n$ and redefined as a boundary value problem. Let E_i^n be the union of all cells belonging to the stencil $\mathcal{S}_i^n$ centered on cell Ω_i^n identified by the cell-center $\boldsymbol{x}_i^n$ (i.e., $E_i^n = \Omega_i^n \cup \bigcup_{j \in \mathcal{S}_i^n} \Omega_j^n$). Function $\Pi_i \phi$ is the polynomial interpolation of a given function $\phi \in C^2(E_i^n)$, whose knowledge is only available to the cell-centers, by employing the quadratic basis of the polynomial space function

$$\mathcal{P}_2(E_i^n) = \text{span}\left\{ 1, x - x_i^n, y - y_i^n, (x - x_i^n)(y - y_i^n), \frac{1}{2}(x - x_i^n)^2, \frac{1}{2}(y - y_i^n)^2 \right\}.$$

We remark that at this stage the face-centered velocity field $\boldsymbol{U}$ is not required as originally indicated in problem (7).

In order to refer problem (12) to the reference domain $\hat{\mathcal{C}}$, we use a map $\mathcal{M}_i : \hat{\mathcal{C}} \to \mathcal{C}_i^n$

$$\mathcal{M}_i : \begin{cases} x = x(\xi, \eta, \tau) \\ y = y(\xi, \eta, \tau) \\ t = t^n + \Delta t\,\tau \end{cases}, \tag{13}$$

such that any space-time point $\boldsymbol{x} \equiv (x, y, t)$ in the physical space-time cell $\mathcal{C}_i^n$ is a function $\boldsymbol{x} = \boldsymbol{x}(\boldsymbol{\xi})$, with $\boldsymbol{\xi} \in \hat{\mathcal{C}}$ (see Figure 4). Time t is considered as linear function of τ of slope Δt. From map (13), the Jacobian matrix J reads

$$J = \frac{\mathrm{d}\boldsymbol{x}}{\mathrm{d}\boldsymbol{\xi}} = \begin{bmatrix} x_\xi & x_\eta & x_\tau \\ y_\xi & y_\eta & y_\tau \\ 0 & 0 & \Delta t \end{bmatrix}, \tag{14}$$

whose inverse is

$$J^{-1} = \frac{\mathrm{d}\boldsymbol{\xi}}{\mathrm{d}\boldsymbol{x}} = \begin{bmatrix} \xi_x & \xi_y & \xi_t \\ \eta_x & \eta_y & \eta_t \\ 0 & 0 & 1/\Delta t \end{bmatrix}. \tag{15}$$

Moreover, let J_s^{-1} be the restriction to the spatial coordinates of the inverse of the Jacobian matrix (15):

$$J_s^{-1} = \begin{bmatrix} \xi_x & \xi_y \\ \eta_x & \eta_y \end{bmatrix}. \tag{16}$$

Through (16), the problem in the reference domain reads[1]

$$\partial_\tau q_k + \Delta t \mathcal{F}^\flat(\hat\nabla q_k) + \Delta t\, J_s^{-T}\hat\nabla \cdot \boldsymbol{\mathcal{F}}^\sharp(q_k, \hat\nabla q_k) = 0 \quad \text{in } \hat{\mathcal{C}}, \tag{17}$$

with

$$\mathcal{F}^\flat(\hat\nabla q_k) = \begin{bmatrix} \xi_t \\ \eta_t \end{bmatrix} \cdot \hat\nabla q_k; \quad \boldsymbol{\mathcal{F}}^\sharp(q_k, \hat\nabla q_k) = \boldsymbol{F}(q_k, J_s^{-T}\hat\nabla q_k) = \begin{bmatrix} \mathcal{F}^\sharp_\xi \\ \mathcal{F}^\sharp_\eta \end{bmatrix}; \quad \hat\nabla = \begin{bmatrix} \partial_\xi \\ \partial_\eta \end{bmatrix}.$$

The hat differential operators refer to the reference space variables ξ and η in the reference space-time cell $\hat{\mathcal{C}}$. By abuse of notation and for the sake of simplicity, the solutions q_k involved in both equations (12) and (17) are defined with the same symbol even though they take inputs in the physical space-time cell $\mathcal{C}_i^n$ and in the reference space-time cell $\hat{\mathcal{C}}$, respectively. In order to weaken the problem (17), we introduce the following functional space

$$\Theta = \left\{ v \in H^1(\hat{\mathcal{C}}) : [0,1] \ni \tau \mapsto v(\xi,\eta,\tau) = V_\tau(\xi,\eta) \in L^2((0,1)^2) \right\}$$

as subspace of Sobolev space $H^1(\hat{\mathcal{C}})$ of functions that associate a $L^2((0,1)^2)$-integrable function for any fixed reference time τ. Moreover, we use the following notation for any function f and g in Θ:

$$\langle f,g \rangle = \int_{\hat{\mathcal{C}}} fg\, \mathrm{d}\boldsymbol{\xi}; \quad [f,g]_\tau = \int_0^1 \int_0^1 f(\xi,\eta,\tau) g(\xi,\eta,\tau)\, \mathrm{d}\xi \mathrm{d}\eta.$$

Finally, for our purposes, it is identified Θ as a test functional space and a trial functional space Q_k is defined as

$$Q_k = \left\{ v \in \Theta : v(\xi,\eta,0) = \Pi_i u_k^n(x(\xi,\eta,0), y(\xi,\eta,0), t^n) \wedge J^{-1}\begin{bmatrix} \hat\nabla v \\ \partial_\tau v \end{bmatrix} \in L^2(\hat{\mathcal{C}};\mathbb{R}^3) \right\}, \tag{18}$$

where $[J_s^{-1}]_{lm}$, with $l,m = 1,2$, represents the (lm)-component of the spatial inverse Jacobian matrix (16). By multiplying left and right side of (17) by a generic test function θ in Θ and by integrating over the reference space-time cell $\hat{\mathcal{C}}$, the weak problem reads: *find $q_k \in Q_k$ such that*

$$[\theta, q_k]_1 - \langle \partial_\tau \theta, q_k \rangle + \Delta t \langle \theta, \mathcal{F}^\flat(\hat\nabla q_k) \rangle + \Delta t \langle \theta, J_s^{-T}\hat\nabla \cdot \boldsymbol{\mathcal{F}}^\sharp(q_k, \hat\nabla q_k) \rangle = [\theta, \Pi_i u_k^n]_0 \quad \forall \theta \in \Theta. \tag{19}$$

For the above equation, for the solution q_k and the reference convective-diffusive terms $\mathcal{F}^\flat$ and $\boldsymbol{\mathcal{F}}^\sharp$ a Lagrangian polynomial expansion is performed by employing the already presented Lagrange basis, thus, by adopting the Einstein notation, $q_k = \theta_l \hat{q}_{k,l}$ and $\mathcal{F}^\star = \theta_l \mathcal{F}_l^\star$, with $\star = \flat, \sharp$ and $l = 1, \dots, 27$, where $\hat{q}_{k,l} = q_k(\hat{\boldsymbol{\xi}}_l)$ and $\mathcal{F}_l^\star = \mathcal{F}^\star|_{\hat{\boldsymbol{\xi}}_l}$. Considering as test function the m-th Lagrangian polynomial θ_m and by using the Lagrangian expansion, we rewrite the equation (19) as

$$\begin{aligned}
([\theta_m, \theta_l]_1 - \langle \partial_\tau \theta_m, \theta_l \rangle)\hat{q}_{k,l} + \Delta t \langle \theta_m, \theta_l \rangle \hat{\mathcal{F}}_l^\flat + \Delta t \langle \theta_m, (\xi_x \partial_\xi + \eta_x \partial_\eta)\theta_l \rangle \mathcal{F}_{\xi,l}^\sharp \\
+ \Delta t \langle \theta_m, (\xi_y \partial_\xi + \eta_y \partial_\eta)\theta_l \rangle \mathcal{F}_{\eta,l}^\sharp = [\theta_m, \Pi_i u_k^n]_0,
\end{aligned} \tag{20}$$

for any $m = 1, \dots, 27$. In the left hand side of (20), the arising matrices have a sparse pattern due to the L^2-orthogonality of the Lagrangian basis (e.g. the mass matrix by $\langle \theta_m, \theta_l \rangle$ is diagonal). Matrices involving the derivatives of the map $\mathcal{M}_i$, i.e. $\langle \theta_m, (\xi_x \partial_\xi + \eta_x \partial_\eta)\theta_l \rangle$ and $\langle \theta_m, (\xi_y \partial_\xi + \eta_y \partial_\eta)\theta_l \rangle$, cannot be explicitly computed before finding the map itself. On the contrary, the components which do not involve the map, namely $([\theta_m, \theta_l]_1 - \langle \partial_\tau \theta_m, \theta_l \rangle)$ and $\langle \theta_m, \theta_l \rangle$, can be pre-computed once for all before solving problem (20). The above equation (20) is nonlinear due to the convective-diffusive terms $\mathcal{F}^\flat$ and $\boldsymbol{\mathcal{F}}^\sharp$ which depend on the solution q_k. For this reason a fixed point problem is solved: let r be the index of the fixed point iteration, therefore we solve q_k^{r+1}

$$\begin{aligned}
([\theta_m, \theta_l]_1 - \langle \partial_\tau \theta_m, \theta_l \rangle)\hat{q}_{k,l}^{r+1} + \Delta t \langle \theta_m, \theta_l \rangle \hat{\mathcal{F}}_l^{\flat,r} + \Delta t \langle \theta_m, (\xi_x \partial_\xi + \eta_x \partial_\eta)\theta_l \rangle \mathcal{F}_{\xi,l}^{\sharp,r} \\
+ \Delta t \langle \theta_m, (\xi_y \partial_\xi + \eta_y \partial_\eta)\theta_l \rangle \mathcal{F}_{\eta,l}^{\sharp,r} = [\theta_m, \Pi_i u_k^n]_0,
\end{aligned} \tag{21}$$

---

[1]Because of the transformation, it holds

$$\partial_t q_k = \frac{\partial_\tau q_k}{\Delta t} + \mathcal{F}^\flat(\hat\nabla q_k); \quad \text{and} \quad \nabla = J_s^{-T}\hat\nabla.$$

for any $m = 1, \ldots, 27$, where terms of fixed point index r are computed by using the previous solution q_h^r. In our numerical tests, the fixed point iteration stops when the $L^2(\hat{\mathcal{C}})$-norm of residual of equation (21) is less than a fixed tolerance.

In equation (17) the local map $\mathcal{M}_i : \hat{\mathcal{C}} \to \mathcal{C}_i^n$ has been involved for the computation of the local weak predictor solution. The local map is recovered through the movement of the foreground mesh led by the motion equation (3). Otherwise, namely in the background mesh, it is known *a priori*. The motion equation (3) is solved through an *isoparametric* approach by locally referring it to the same reference system as done for the local equation (12). This means that the spatial coordinates $\boldsymbol{X}$ are considered as function of the reference coordinates, i.e. $\boldsymbol{X}(\boldsymbol{\xi})$, with $\boldsymbol{\xi} \in \hat{\mathcal{C}}$. Finally, the solution of the referred motion equation is approximated via a Lagrangian expansion by employing the same Lagrangian basis $\{\theta_m\}_{m=1}^{27}$ built on the tensor combination of three Gauss-Legendre nodes in $(0,1)$ along any direction as previously introduced: $\boldsymbol{X}_h = \theta_l \hat{\boldsymbol{X}}_l$, with $\hat{\boldsymbol{X}}_l = \boldsymbol{X}(\hat{\boldsymbol{\xi}}_l)$. Thus, from time t^n to t^{n+1}, the motion equation (3) is locally re-written as

$$\frac{\mathrm{d}\boldsymbol{X}}{\mathrm{d}t} = \boldsymbol{V} \text{ in } \mathcal{C}_i^n, \tag{22}$$

and closed by strongly imposing that the solution $\boldsymbol{X}^n$ at current time is equal to $\boldsymbol{X}(t^n)$ found at the previous physical space-time cell $\mathcal{C}_i^{n-1}$. The local motion equation (22) is weaken in a similar way to the local equation (12) and in algebraic form it reads

$$([\theta_m, \theta_l]_1 - \langle \partial_\tau \theta_m, \theta_l \rangle) \hat{\boldsymbol{X}}_l = \Delta t \langle \theta_m, \theta_l \rangle \hat{\boldsymbol{V}}_l + [\theta_m, \theta_l]_0 \hat{\boldsymbol{X}}_l^n, \tag{23}$$

for any $m = 1, \ldots, 27$, with $\hat{\boldsymbol{V}}_l = \boldsymbol{V}|_{\hat{\boldsymbol{\xi}}_l}$. The last term $[\theta_m, \theta_l]_0 \hat{\boldsymbol{X}}_l^n$ takes into account the initial given configuration of the space at time t^n.

When the mesh is neither moving nor deforming, as for cells in the background, the mesh velocity is thus coincident with zero, i.e. $\boldsymbol{V} \equiv \boldsymbol{0}$. In that case, the map is known *a priori* and it consists in the rescaling of the reference space-time cell $\hat{\mathcal{C}}$ to the physical space-time cell $\mathcal{C}_i^n$:

$$\begin{cases} x = x(\xi) = x_{i-1/2} + h_i^x \xi \\ y = y(\eta) = y_{i-1/2} + h_i^y \eta \end{cases}, \tag{24}$$

where coordinates $x_{i-1/2}$ and $y_{i-1/2}$ and $x_{i+1/2}$ and $y_{i+1/2}$ define the extremes along x- and y-direction of the physical space-time cell $\mathcal{C}_i^n \equiv [x_{i-1/2}, x_{i+1/2}] \times [y_{i-1/2}, y_{i+1/2}] \times [t^n, t^{n+1}]$; and h_i^x and h_i^y are the length along x and y of the cell, respectively, i.e. $h_i^x = x_{i+1/2} - x_{i-1/2}$ and $h_i^y = y_{i+1/2} - y_{i-1/2}$.

Since the mesh motion equation (3) is essentially solved via a sort of Discontinuous Galerkin (DG) approach, possible numerical (and non physical) discontinuities could arise. As a matter of fact, for a given vertex $\bar{\boldsymbol{X}}_j^{n+1}$ shared by a set of spatial cells $\{\Omega_i^{n+1}\}_{i \in \mathcal{Z}_j^{n+1}}$ at time t^{n+1}, there could be as many different values of the vertex, namely $\{\bar{\boldsymbol{X}}_{j,i}^{n+1}\}_{i \in \mathcal{Z}_j^{n+1}}$, for any map $\mathcal{M}_i$ referring to the cell $\mathcal{C}_i^n$ to which Ω_i^{n+1} belongs. The set $\mathcal{Z}_j^{n+1}$ collects the index(es) of the cells sharing the vertex $\bar{\boldsymbol{X}}_j^{n+1}$. The cardinality N_j of set $\{\Omega_i^{n+1}\}_{i \in \mathcal{Z}_j^{n+1}}$, coinciding with the cardinality of the indexes set $\mathcal{Z}_j^{n+1}$, depends on the position of the vertex $\bar{\boldsymbol{X}}_j^{n+1}$ on the foreground mesh: it is either 1 or 2 if the vertex is on the boundary of the mesh, otherwise it is 4, if the topology of the cell is quadrilateral. For this reason we consider a weighted average value for the shared vertex in order to tackle the possible arising discontinuities. As suggested in [30], we first consider a weighted velocity $\bar{\boldsymbol{V}}_j^{n+1}$ corresponding to the vertex $\bar{\boldsymbol{X}}_j^{n+1}$

$$\bar{\boldsymbol{V}}_j^{n+1} = \frac{1}{N_j} \sum_{i \in \mathcal{Z}_j^{n+1}} \bar{\boldsymbol{V}}_{j,i}^{n+1}, \text{ with } \bar{\boldsymbol{V}}_{j,i}^{n+1} = \int_0^1 \theta_l(\xi^*, \eta^*, \tau) \, \mathrm{d}\tau \, \hat{\boldsymbol{V}}_{l,i}, \tag{25}$$

where coordinates (ξ^*, η^*) depend on the position of the coordinate $\bar{\boldsymbol{X}}_j^{n+1}$ in the cell Ω_i^{n+1}; it can assume four values: $(0,0)$, $(1,0)$, $(1,1)$ and $(0,1)$. Once equation (23) is solved, the just found coordinates $\{\hat{\boldsymbol{X}}_l\}_{l=1}^{27}$

are used for computing the velocity components $\hat{\boldsymbol{V}}_{l,i}$ and, thus, the weighted velocities $\bar{\boldsymbol{V}}_j^{n+1}$ in (25). Finally, the coordinates $\bar{\boldsymbol{X}}_j^{n+1}$ at time t^{n+1} is

$$\bar{\boldsymbol{X}}_j^{n+1} = \bar{\boldsymbol{X}}_j^n + \Delta t \, \bar{\boldsymbol{V}}_j^{n+1}. \tag{26}$$

For another definition of the weighted vertex velocities $\bar{\boldsymbol{V}}_j^{n+1}$ in (25) by exploiting the Voronoi neighborhood parameters of any vertex, the reader is addressed to [20] .
In Algorithm 2 we resume the salient stages of the prediction step.

Algorithm 2 Prediction step

1: Compute the foreground mesh motion (26) from the motion equation (3) and through the weighted velocity (25);
2: **for** $i = 1, \ldots, N$ **do**
3:     Find the map $\mathcal{M}_i$ for the space-time cell $\mathcal{C}_i^n$;
4:     Compute (14), the Jacobian matrix J associated to $\mathcal{M}_i$;
5:     Compute J^{-1} and take the submatrix J_s^{-1} as defined in (16);
6:     Update the convective-diffusive terms $\mathcal{F}^{\flat}$ and $\boldsymbol{\mathcal{F}}^{\sharp}$ in the reference domain;
7:     Evolve the local predictor solution through (20);

4.1.2   The space-time finite volume scheme

Once the local predictor solution q_k is computed in each space-time cells $\mathcal{C}_i^n$, we can perform the ADER correction stage. First, we rewrite the convective-diffusive equation (7) in divergence form. Let $\boldsymbol{F}_{\boldsymbol{U}^n}(u_k^*, \nabla u_k^*) = \boldsymbol{U}^n u_k^* - \nabla u_k^*/\text{Re}$, with $k = 1, 2$, be the convective-diffusion term associated to the component-wise equation (7); let $\nabla_{\boldsymbol{x},t} = [\nabla, \partial_t]^T$ be the space-time differential operator and, finally, let $\boldsymbol{\mathcal{U}}_k = [\boldsymbol{F}_{\boldsymbol{U}^n}(u_k^*, \nabla u_k^*), u_k^*]^T$, $k = 1, 2$, be the k-component of the space-time solution, thus problem (7) can be rewritten as: *for any* $k = 1, 2$,

$$\nabla_{\boldsymbol{x},t} \cdot \boldsymbol{\mathcal{U}}_{\boldsymbol{k}} = 0 \quad \text{in } \Omega(t) \times (0, T). \tag{27}$$

the objective is to find a finite volume solution for the above equation, where the finite volume is the space-time cell $\mathcal{C}_i^n$, whose boundary reads

$$\partial \mathcal{C}_i^n = \Omega_i^n \cup \Omega_i^{n+1} \cup \bigcup_{j=1}^4 \Gamma_{ij}^n, \tag{28}$$

where the boundaries Γ_{ij}^n, $j = 1, \ldots, 4$, are the space-time boundaries of $\mathcal{C}_i^n$ linking any edge of Ω_i^n at time t^n to any edge of Ω_i^{n+1} at time t^{n+1} (see the sketch of the physical space-time cell in Figure 4). By integrating equation (27) over $\mathcal{C}_i^n$ and by applying the divergence theorem to the left side, we obtain

$$\oiint_{\partial \mathcal{C}_i^n} \boldsymbol{\mathcal{U}}_{\boldsymbol{k}}^{\boldsymbol{n}} \cdot \boldsymbol{n}_{\boldsymbol{x},t} \, \mathrm{d}\Gamma = 0, \tag{29}$$

with $\boldsymbol{n}_{\boldsymbol{x},t} = [\boldsymbol{n}_{\boldsymbol{x}}, n_t]^T = [n_x, n_y, n_t]^T$ being the normal unit vector to the boundary $\partial \mathcal{C}_i^n$ of the cell. Let $\bar{u}_{k,i}^{*,n}$ be the spatial average solution u_k^* cell-centered in the space cell Ω_i^n at time t^n, i.e.,

$$\bar{u}_{k,i}^{*,n} = \frac{1}{|\Omega_i^n|} \int_{\Omega_i^n} u_k^*(x, y, t^n) \, \mathrm{d}x \, \mathrm{d}y, \tag{30}$$

where $|\Omega_i^n|$ is the measure of the spatial cell Ω_i^n. Though (28) and (30), equation (29) explicitly is

$$-|\Omega_i^n|\bar{u}_{k,i}^{*,n} + |\Omega_i^{n+1}|\bar{u}_{k,i}^{*,n+1} + \sum_{j=1}^4 \int_{\Gamma_{ij}^n} \boldsymbol{\mathcal{U}}_k \cdot \boldsymbol{n}_{\boldsymbol{x},t} \, \mathrm{d}\Gamma = 0, \tag{31}$$

where the unknown is the average solution $\bar{u}_{k,i}^{*,n+1}$ at time t^{n+1}, while the last term of the left hand side is the space-time flux along the space-time sides $\bigcup_{j=1}^{4} \Gamma_{ij}^{n}$. Scheme (31) is the space-time Finite Volume scheme; we remark that it is still exact. In order to solve (31), the integral function of the space-time flux is approximated through a Local Lax-Friederichs (LLF) approach:

$$[\boldsymbol{\mathcal{U}}_k \cdot \boldsymbol{n}_{\boldsymbol{x},t}]_{\Gamma_{ij}^n} \approx \Phi(q_{k,j}^+, q_{k,j}^-) = \frac{1}{2}(\boldsymbol{\mathcal{U}}_{k,j}^+ + \boldsymbol{\mathcal{U}}_{k,j}^-) \cdot \boldsymbol{n}_{\boldsymbol{x},t} - \frac{s}{2}(q_{k,j}^+ - q_{k,j}^-), \tag{32}$$

where $\boldsymbol{\mathcal{U}}_{k,j}^+ = \boldsymbol{\mathcal{U}}_{k,j}(q_{k,j}^+)$ and $\boldsymbol{\mathcal{U}}_{k,j}^- = \boldsymbol{\mathcal{U}}_{k,j}(q_{k,j}^-)$ are the space-time solution of (27) computed by solutions $q_{k,j}^+$ and $q_{k,j}^-$, which represent the local predictor solutions outside and inside the cell, respectively, with respect to the space-time side Γ_{ij}^n. The term s is the local stabilization coefficient depending on the face-centered velocity $\boldsymbol{U}^n$ considered constant over the space-time side Γ_{ij}^n. It reads

$$s = \frac{1}{2}\left| \boldsymbol{U}^n \cdot \boldsymbol{n}_{\boldsymbol{x}} + 2n_t + \sqrt{\left[(U_x^n)^2 + \frac{4}{\varepsilon \mathrm{Re}}\right] n_x^2 + 2U_x^n U_y^n n_x n_y + \left[(U_y^n)^2 + \frac{4}{\varepsilon \mathrm{Re}}\right] n_y^2} \right|, \tag{33}$$

where ε is a relaxation parameter. In order to ensure a second-order convergence for the scheme, the relaxation term ε is chosen to be smaller than an optimal relaxation parameter ε_2 [31, 32] defined as

$$\varepsilon_2 = \frac{\mathcal{O}(1)h_{\max}^2}{C_2}, \tag{34}$$

where $h_{\max}$ is the maximum characteristic length among all the cells and $C_2 = (1 - 2^{-1/2})/(2^{-3/2} - 1)$ is a parameter depending on the convergence rate of the scheme. In particular, the relaxation parameter ε is set as $\varepsilon_2/2$. For further details, the reader is referred to [24] and its references.

Equation (31) with the flux approximation (32) closes the correction stage of the ADER method. At the end of this stage, the cell-centered k-th component of the solution $u_{k,i}^{*,n+1}$ is found over any cell Ω_i^{n+1} at time t^{n+1}.

4.2 The pressure equation

The second step of the fractional method is the projection step defined by the Poisson equation (10) for pressure $\psi^{n+1} = \Delta t \, p^{n+1}$ at time t^{n+1} on the Chimera configuration for the domain Ω^{n+1}. In this section, in order to lighten the notation, the reference to time t^{n+1} is omitted for all involved variables and quantities. Let the stencil $\mathcal{S}_i$ centered on cell Ω_i be decomposed in $\mathcal{S}_i = \mathcal{S}_i^+ \cup \mathcal{S}_i^\times$, with $\mathcal{S}_i^+$ of cells sharing either one or no edge with Ω_i and $\mathcal{S}_i^\times$ the remaining cells sharing only one vertex of Ω_i. The proposed scheme for (10) is a spatial FV approach. Thus, by integrating over the space cell Ω_i, whose boundary is $\partial\Omega_i = \bigcup_{j \in \mathcal{S}_i^+} \gamma_{ij}$, and by applying the divergence theorem both to the left and right hand sides, the problem exactly reads

$$\sum_{j \in \mathcal{S}_i^+} \int_{\gamma_{ij}} \nabla\psi \cdot \boldsymbol{n}_{ij} \, \mathrm{d}\gamma = - \sum_{j \in \mathcal{S}_i^+} \int_{\gamma_{ij}} \boldsymbol{U}^* \cdot \boldsymbol{n}_{ij} \, \mathrm{d}\gamma, \tag{35}$$

with $\boldsymbol{n}_{ij}$ the unit outer normal to side γ_{ij}. The integrals in (35) are approximated as

$$\sum_{j \in \mathcal{S}_i^+} |\gamma_{ij}| [\nabla\psi \cdot \boldsymbol{n}]_{ij} = - \sum_{j \in \mathcal{S}_i^+} |\gamma_{ij}| \boldsymbol{U}_{ij}^* \cdot \boldsymbol{n}_{ij}, \tag{36}$$

where $|\gamma_{ij}|$ is the length of side γ_{ij}. In order to achieve the Poisson algebraic system for problem (36), the approximation of the face-centered normal divergence term $[\nabla\psi \cdot \boldsymbol{n}]_{ij}$ along γ_{ij} is needed. For this reason, two different strategies are adopted with respect to the position of the spatial cell Ω_i: if the cell is not *fringe*, namely it is not at the boundary of the overlapping interface of its partition, the approximation is performed through a *geometric* reconstruction, otherwise, an *analytic* approach is employed.
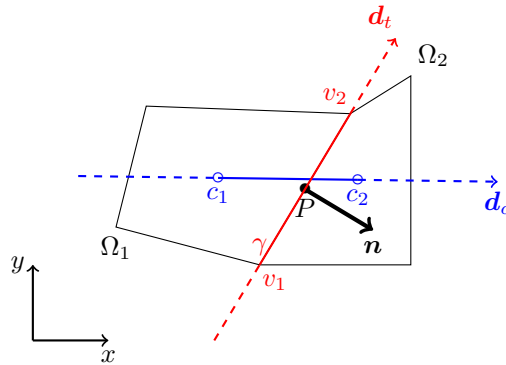
Figure 5: Sketch of two internal cells Ω_1 and Ω_2 sharing the edge γ.

4.2.1   The geometric reconstruction

By considering Figure 5, let us consider two internal cells Ω_1 and Ω_2 in the same partition and sharing the edge γ of normal $\boldsymbol{n}$. Let P be the face-center of γ. Moreover, let $\boldsymbol{c}_1$ and $\boldsymbol{c}_2$ be the cell-centers of the two cells and $\boldsymbol{v}_1$ and $\boldsymbol{v}_2$ be the extremes of edge γ. These points define the unit direction vectors $\boldsymbol{d}_c$ (of the centers) and $\boldsymbol{d}_t$ (tangent), respectively. The objective is to approximate the normal gradient $[\nabla\psi \cdot \boldsymbol{n}]_P$, applied on P, assumed to be constant over γ. It is approximated via the *diamond formula* [25, 26] as

$$[\nabla\psi \cdot \boldsymbol{n}]_P \approx \frac{1}{\boldsymbol{d}_c \cdot \boldsymbol{n}}\left(\frac{\psi_{c_2} - \psi_{c_1}}{|\boldsymbol{c}_2 - \boldsymbol{c}_1|} - \frac{\psi_{v_2} - \psi_{v_1}}{|\gamma|}\,\boldsymbol{d}_c \cdot \boldsymbol{d}_t\right). \tag{37}$$

In the above approximation, due to the cell-centered nature of the scheme, an approximation of the vertex-centered quantities ψ_{v_1} and ψ_{v_2} are necessary. In particular, they have to be expressed as function of some cell-centered quantities of the unknown pressure ψ. Let us study this approximation for vertex $\boldsymbol{v}_1$; the extension to vertex $\boldsymbol{v}_2$ trivially follows. Let $\tilde{\mathcal{S}}_{v_1}$ be the substencil of indexes of those cells sharing vertex $\boldsymbol{v}_1$. For internal cells, the cardinality of substencil $\tilde{\mathcal{S}}_{v_1}$ is equal to 4. Thus, let $\tilde{E}_{v_1} = \bigcup_{j \in \tilde{\mathcal{S}}_{v_1}} \Omega_j$ be the subdomain composed of cells sharing the vertex $\boldsymbol{v}_1$. Finally, let $\tilde{\Pi}_{v_1}\phi$ be the polynomial interpolation of a given function $\phi \in C^2(\tilde{E}_{v_1})$, whose knowledge is available to the cell-centers, by employing the bilinear basis of the polynomial space function $\mathcal{Q}_1^0 = \text{span}\{1, x, y, xy\}$. In particular, it holds that

$$\tilde{\Pi}_{v_1}\psi(x, y) = \alpha_{v_1,1} + \alpha_{v_1,2}x + \alpha_{v_1,3}y + \alpha_{v_1,4}xy = \boldsymbol{z}^T\boldsymbol{\alpha}_{v_1},$$

with $\boldsymbol{z} = [1, x, y, xy]^T$ and the unknown polynomial coefficients collected in vector $\boldsymbol{\alpha}_{v_1}$. The polynomial coefficients are looked for by imposing that the polynomial equals the pressure at the cell-centers of the substencil (i.e., $\tilde{\Pi}_{v_1}\psi(x_j, y_j) \equiv \psi_j$ for any j in $\tilde{\mathcal{S}}_{v_1}$). This yields the resolution of linear system $A_{v_1}\boldsymbol{\alpha}_{v_1} = \boldsymbol{\psi}_{v_1}$, where the row space of $A_{v_1} \in \mathbb{R}^{4\times4}$ is defined by the coordinates in $\boldsymbol{z}_j$ and vector $\boldsymbol{\psi}_{v_1}$ collects the cell-centered values ψ_j, with $j \in \tilde{\mathcal{S}}_{v_1}$. Finally we approximate as follows:

$$\psi_{v_1} \approx \tilde{\Pi}_{v_1}\psi(x_{v_1}, y_{v_1}) = \boldsymbol{z}_{v_1}^T\boldsymbol{\alpha}_{v_1} = \boldsymbol{z}_{v_1}^T A_{v_1}^{-1}\boldsymbol{\psi}_{v_1}, \tag{38}$$

that only depends on cell-centered values of ψ. This allows to finally define the i-th line of system for problem (36). The scheme for internal cells reads

$$\sum_{j \in \mathcal{S}_i^+} \frac{|\gamma_{ij}|}{\boldsymbol{d}_{c_{ij}} \cdot \boldsymbol{n}_{ij}}\left(\frac{\psi_j - \psi_i}{|\boldsymbol{c}_j - \boldsymbol{c}_i|} - \frac{\boldsymbol{z}_{v_{2j}}^T A_{v_{2j}}^{-1}\boldsymbol{\psi}_{v_{2j}} - \boldsymbol{z}_{v_{1j}}^T A_{v_{1j}}^{-1}\boldsymbol{\psi}_{v_{1j}}}{|\gamma_{ij}|}\,\boldsymbol{d}_{c_{ij}} \cdot \boldsymbol{d}_{v_{ij}}\right) = \sum_{j \in \mathcal{S}_i^+} |\gamma_{ij}|\boldsymbol{U}_{ij}^* \cdot \boldsymbol{n}_{ij}, \tag{39}$$

where the unknowns are the cell-centered values of ψ.

4.2.2 Truncation error and stencil at fringe cells

For the fringe cells, the diamond formula (37) for approximating the normal gradient in (35) is more complicated. In fact there exists at least one edge for which the second center $\boldsymbol{c}_2$ falls in the other partition. Thus, in a generic configuration, it could be happen that the center direction $\boldsymbol{d}_c$ tends to be parallel to the tangent direction $\boldsymbol{d}_t$, implying a vanishing term $\boldsymbol{d}_c \cdot \boldsymbol{n}$. The approach that we adopt exploits the analytic information stored in any stencil $\mathcal{S}_i$ centered on cell Ω_i. Let $\mathcal{R}_i = \mathcal{S}_i \cup \{i\}$ be the increased stencil which includes also the index i. Let P the generic face-centered point on which the pressure gradient needs to be approximated. In the sequel we provide the gradient approximation along the x-direction; the approximation along y similarly follows. For any j in $\mathcal{R}_i$, the Taylor polynomial expansion of ψ_j with respect to the face-centered value ψ_P truncated to the second-order terms is

$$\psi_j = \psi_P + h_j^x \partial_x \psi_P + h_j^y \partial_y \psi_P + h_j^x h_j^y \partial_{xy}^2 \psi_P + \frac{1}{2}(h_j^x)^2 \partial_{xx}^2 \psi_P + \frac{1}{2}(h_j^y)^2 \partial_{yy}^2 \psi_P + \mathcal{O}(H_j^3), \qquad (40)$$

with $h_j^x = x_j - x_P$, $h_j^y = y_j - y_P$ and $H_j = \max\{|h_j^x|, |h_j^y|\}$. As done in the previous subsection, the objective is to represent the face-centered gradient as dependent on the cell-centered quantity in the stencil, i.e.,

$$\partial_x \psi_P = \sum_{j \in \mathcal{R}_i} \beta_{\mathfrak{s}P(j)}^x \psi_j, \qquad (41)$$

with coefficients $\beta_{\mathfrak{s}P(j)}^x$ to be found. The discrete function $\mathfrak{s}_P : \mathcal{R}_i \to \{1, \dots, m\}$, with $m = |\mathcal{R}_i|$ being the cardinality of the enlarged stencil, sorts the indexes in $\mathcal{R}_i$ in increasing order. By plugging the Taylor truncated expansion (40) in (41), it holds:

$$\partial_x \psi_P = \left(\sum_{j \in \mathcal{R}_i} \beta_{\mathfrak{s}P(j)}^x \right) \psi_P + \left(\sum_{j \in \mathcal{R}_i} \beta_{\mathfrak{s}P(j)}^x h_j^x \right) \partial_x \psi_P + \left(\sum_{j \in \mathcal{R}_i} \beta_{\mathfrak{s}P(j)}^y h_j^y \right) \partial_y \psi_P + \left(\sum_{j \in \mathcal{R}_i} \beta_{\mathfrak{s}P(j)}^x h_j^x h_j^y \right) \partial_{xy}^2 \psi_P$$
$$+ \left(\sum_{j \in \mathcal{R}_i} \frac{1}{2} \beta_{\mathfrak{s}P(j)}^x (h_j^x)^2 \right) \partial_{xx}^2 \psi_P + \left(\sum_{j \in \mathcal{R}_i} \frac{1}{2} \beta_{\mathfrak{s}P(j)}^x (h_j^x)^2 \right) \partial_{xx}^2 \psi_P + \mathcal{O}\left(\max_{j \in \mathcal{R}_i} H_j^3 \right). \qquad (42)$$

Since the right side of (42) is the approximation of the x-derivative of ψ_P, the condition on the coefficients $\beta_{\mathfrak{s}P(j)}^x$ are

$$\sum_{j \in \mathcal{R}_i} \beta_{\mathfrak{s}P(j)}^x = 0; \qquad \sum_{j \in \mathcal{R}_i} \beta_{\mathfrak{s}P(j)}^x h_j^x = 1; \qquad \sum_{j \in \mathcal{R}_i} \beta_{\mathfrak{s}P(j)}^x h_j^y = 0;$$
$$\sum_{j \in \mathcal{R}_i} \beta_{\mathfrak{s}P(j)}^x h_j^x h_j^y = 0; \quad \sum_{j \in \mathcal{R}_i} \frac{1}{2} \beta_{\mathfrak{s}P(j)}^x (h_j^x)^2 = 0; \quad \sum_{j \in \mathcal{R}_i} \frac{1}{2} \beta_{\mathfrak{s}P(j)}^x (h_j^y)^2 = 0; \qquad (43)$$

which can be synthesized in the linear system $M\boldsymbol{\beta}^x = \boldsymbol{b}^x$, with $M \in \mathbb{R}^{6 \times m}$, $\boldsymbol{\beta}^x \in \mathbb{R}^m$, $\boldsymbol{b}^x \in \mathbb{R}^6$. Similar consideration can be assumed for the approximation of the y-derivative. For this reason, for now we consider the generic system

$$M\boldsymbol{\beta} = \boldsymbol{b}. \qquad (44)$$

Inspired by [27], for a general value of m, system (44) is solved by minimizing a Lagrangian function under the constraints defined by a convex function $\mathcal{H} : \mathbb{R}^m \to \mathbb{R}$. Let $\boldsymbol{\lambda} \in \mathbb{R}^\nu$ be a vector of Lagrangian multipliers. Moreover let $\mathcal{L} : \mathbb{R}^m \times \mathbb{R}^\nu \to \mathbb{R}$ be the Lagrangian function to be minimized defined as

$$\mathcal{L}(\boldsymbol{\beta}, \boldsymbol{\lambda}) = \mathcal{H}(\boldsymbol{\beta}) - \boldsymbol{\lambda}^T (M\boldsymbol{\beta} - \boldsymbol{b}). \qquad (45)$$

To minimize this function means to find the stationary point $(\boldsymbol{\beta}, \boldsymbol{\lambda})$ such that

$$\begin{cases} \frac{\partial \mathcal{L}}{\partial \boldsymbol{\beta}} = \boldsymbol{0} \\ \frac{\partial \mathcal{L}}{\partial \boldsymbol{\lambda}} = \boldsymbol{0} \end{cases} \iff \begin{cases} \frac{\partial \mathcal{H}}{\partial \boldsymbol{\beta}} - M^T \boldsymbol{\lambda} = \boldsymbol{0} \\ M\boldsymbol{\beta} = \boldsymbol{b} \end{cases}. \qquad (46)$$

Let $C \in \mathbb{R}^{4 \times m}$ be the sub-matrix relative to the second-order constraints. Two cases are distinguished:
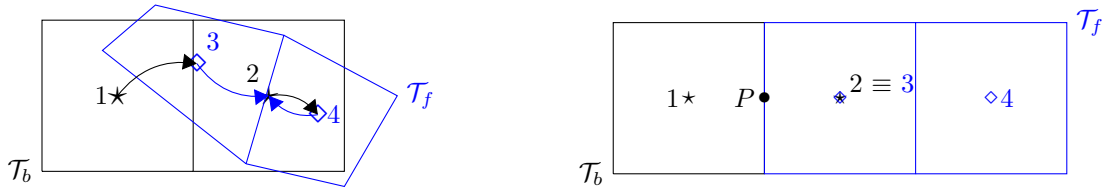
(a) In this configuration it holds: $a_{bf}(\{1,2\}) = \{3,4\}$ while $a_{fb}(\{3,4\}) = \{2\}$.

(b) No-shift configuration. It holds: $a_{bf}(2) = 3 = a_{fb}^{-1}(2)$, $a_{fb}(3) = 2 = a_{bf}^{-1}(3)$ and $\Omega_2 \equiv \Omega_3$.

Figure 6: Sketch of overlapping configurations. Black cells $\{1,2\}$ belong to the background partitions, blue cells $\{3,4\}$ to the foreground. The star symbols ($\star$) and the diamond symbols ($\diamond$) represent the cell-centers for cells in the background and in the foreground, respectively.

$m \leq 10$: The convex function is $\mathcal{H}(\boldsymbol{\beta}) = 1/2\boldsymbol{\beta}^T[(1-\delta)C^TC + \delta G]\boldsymbol{\beta}$, with $\nu = 6$, consequently the local system to be solved is

$$\begin{bmatrix} [(1-\delta)C^TC + \delta G] & -M^T \\ M & O \end{bmatrix} \begin{bmatrix} \boldsymbol{\beta} \\ \boldsymbol{\lambda} \end{bmatrix} = \begin{bmatrix} \mathbf{0} \\ \boldsymbol{b} \end{bmatrix}, \tag{47}$$

where O is the null matrix in $\mathbb{R}^{6\times 6}$. This choice of the convex function $\mathcal{H}(\boldsymbol{\beta})$ is such that the discretization coefficients minimize the second-order truncation error encoded in matrix M and their L^∞-norm is penalised by coefficient δ (which is put equal to 0.01 in the presented test cases) in that region of the stencil indicated by matrix $G \in \mathbb{R}^{m\times m}$, as it will be later discussed.

$m > 10$: The convex function reads $\mathcal{H}(\boldsymbol{\beta}) = 1/2\boldsymbol{\beta}^T\boldsymbol{\beta}$ and $\nu = 10$. Thus the local minimization system is

$$\begin{bmatrix} I & -\tilde{M}^T \\ \tilde{M} & O \end{bmatrix} \begin{bmatrix} \boldsymbol{\beta} \\ \mathbf{0} \end{bmatrix} = \begin{bmatrix} \mathbf{0} \\ \boldsymbol{b} \end{bmatrix}, \tag{48}$$

with $\tilde{M} = \begin{bmatrix} M \\ C \end{bmatrix}$ and I is the identity matrix in $\mathbb{R}^{10\times 10}$. In this case the coefficients satisfy 10 second-order accuracy constraints while their norm is minimized.

The scheme for the fringe cells is

$$\sum_{j\in\mathcal{S}_i^+} |\gamma_{ij}| \sum_{l\in\mathcal{R}_i} (\beta^x_{\mathfrak{s}_{ij}(l)} n_{x,ij} + \beta^y_{\mathfrak{s}_{ij}(l)} n_{y,ij})\psi_l = \sum_{j\in\mathcal{S}_i^+} |\gamma_{ij}| \boldsymbol{U}^*_{ij} \cdot \boldsymbol{n}_{ij}, \tag{49}$$

where the unknowns are the cell-centered values of ψ.

One goal for numerically solving the pressure problem is to have the same scheme for fringe and internal cells in the limit of a perfect no-shift overlapping between the background and foreground meshes. This allows to properly control the fluxes exiting from the background and entering in the foreground (and *vice versa*) and, consequently, to have a conservative scheme at least in this limit condition.

Let $\mathcal{O}$ be the set of indexes for cells in the overlapping zone. It is possible to separate this set in two sets $\mathcal{O}_b$ and $\mathcal{O}_f$ for the background and foreground, respectively, such that $\mathcal{O} = \mathcal{O}_b \cup \mathcal{O}_f$ and $\mathcal{O}_b \cap \mathcal{O}_f = \emptyset$. Moreover, let $a_{bf} : \mathcal{O}_b \to \mathcal{O}_f$ (and $a_{fb} : \mathcal{O}_f \to \mathcal{O}_b$) be the function associating the closest background (foreground) overlapping cell to a given foreground (background) overlapping cell, i.e., for any $i \in \mathcal{O}_b$ (and $j \in \mathcal{O}_f$)

$$a_{bf}(i) = \arg \min_{j\in\mathcal{O}_f} |\boldsymbol{x}_i - \boldsymbol{x}_j| \quad \left(\text{and } a_{fb}(j) = \arg \min_{i\in\mathcal{O}_b} |\boldsymbol{x}_j - \boldsymbol{x}_i|\right). \tag{50}$$

In a general overlapping configuration, it holds that $a_{fb}^{-1} \neq a_{bf}$ and $a_{bf}^{-1} \neq a_{fb}$, as it is showed in Figure 6a. Through the association functions it is possible to formalize the no-shift overlapping limit configuration.

Definition 4.1 (No-shif overlapping configuration) *The overlapping configuration is said to be no-shift when it holds both*

$$a_{bf} = a_{fb}^{-1} \quad or \quad a_{fb} = a_{bf}^{-1}; \tag{51a}$$

$$\forall i \in \mathcal{O}_b \quad \exists! j = a_{bf}(i) \in \mathcal{O}_f \quad such \ that \quad i = a_{fb}(j) \quad and \quad \overline{\Omega_i \cap \Omega_j} = \overline{\Omega}_k, \ with \ k = i, j. \tag{51b}$$

The limit of no-shift condition takes place when all overlapping cells in the background perfectly coincide with all overlapping foreground cells in the foreground with a one-to-one match defined by the associations functions (an example is sketched in Figure 6b).

Let us consider a fringe cell Ω_i in a no-shift overlapping configuration for uniform Cartesian meshes of characteristic length h and let us suppose to compute the gradient at the face-center P of the side after which there is cell Ω_j not belonging to the same partition of Ω_i (as in Figure 6b for cells Ω_3, fringe, and Ω_1, internal). If the diamond formula (37) is used in this case, the tangential contribution vanishes because $\boldsymbol{d}_c \cdot \boldsymbol{d}_t = 0$, consequently, the diamond formula corresponds to the minimization of the Lagrangian functional associated to problem (44) fulfilling the second-order constraints (43) with coefficients: $\beta_{\mathfrak{s}_{ij}(i)} = -\beta_{\mathfrak{s}_{ij}(j)} = -1/h$ and $\beta_{\mathfrak{s}_{ij}(k)} = 0$ for any $k \in \mathcal{R}_i/\{i,j\}$. This means that the diamond formula in the view of the problem defined by (47) is minimizing the L^∞-norm of the local parameters only in those cells of the stencil sufficiently far from the face-center point P (where the value of the local coefficients is put to 0). Consequently, all the information for the reconstruction of the gradient is recovered from the closest cells to P. This concept is encoded in matrix G defined as a diagonal matrix $G = \mathrm{diag}(g_{\mathfrak{s}_{ij}(k)})_{k \in \mathcal{R}_i}$, with the diagonal components defined as

$$g_{\mathfrak{s}_{ij}(k)} = \begin{cases} 1; & k \neq \arg\min_{l \in \mathcal{R}_i} |\boldsymbol{x}_l - \boldsymbol{x}_P| \\ 0; & \text{otherwise} \end{cases}. \tag{52}$$

With this definition, in the considered overlapping configuration, components g_k assume value 1 only for $k \neq i, j$ (thus for all cells whose centers do not minimize the distance with the face-center P) and the solution of problem (47) can be proved to provide $\beta_{\mathfrak{s}_{ij}(i)} = -\beta_{\mathfrak{s}_{ij}(j)} = -1/h$ and $\beta_{\mathfrak{s}_{ij}(k)} = 0$ for any $k \in \mathcal{R}_i/\{i,j\}$, as defined by the diamond formula. When matrix G is put equal to the identity, the L^∞-norm is penalized all over the stencil [27]. In the simulations of this work, matrix G with coefficients defined by (52) is used for any overlapping configuration, allowing to have a unique scheme for internal and fringe cells in the limit of the no-shift overlapping condition.

4.3 The face-center discrete operators on overset grids

Accordingly to the Chorin-Temam scheme presented at the beginning of Section 4, the face-centered values of the velocity and pressure gradient are needed. These computations takes again into account either the internal or fringe position of the cell.

When the intermediate velocity $\boldsymbol{u}^*$ is computed at the end of the predictor step (7), its face-centered counterpart $\boldsymbol{U}^*$ becomes the force term for the pressure equation (10). If the edge is shared by two cells of the same partition, the face-centered approximation is the mean of the $\mathcal{P}_2$-interpolations evaluated on the face-center by using both the stencils of the two involved cells. On the contrary, when the side only belongs to one cell (because it is fringe), the approximation is still the evaluation of the polynomial interpolation on the face-center but just considering the hybrid stencil of the cell.

In the last step (11b) of the fractional step, the face-centered gradient pressure is used to correct the new face-centered velocity. For fringe cells, the face-centered approximation still exploits the local coefficients explained in the Section 4.2.2. For internal cells, through the diamond formula (37), it is possible to approximate the directional derivatives on the face-center along the center and tangential directions. In particular they read

$$\partial_{\boldsymbol{d}_c} \psi \approx \frac{\psi_{c_2} - \psi_{c_1}}{|\boldsymbol{c}_2 - \boldsymbol{c}_1|} \quad \text{and} \quad \partial_{\boldsymbol{d}_t} \psi \approx \frac{\psi_{v_2} - \psi_{v_1}}{|\gamma|}, \tag{53}$$

respectively, where $\partial_{\boldsymbol{d}} \psi = \nabla \psi \cdot \boldsymbol{d}$ is the directional derivative of ψ along direction $\boldsymbol{d}$. Consequently it holds

$$\begin{bmatrix} d_{c,x} & d_{c,y} \\ d_{t,x} & d_{t,y} \end{bmatrix} \begin{bmatrix} \partial_x \psi \\ \partial_y \psi \end{bmatrix} = \begin{bmatrix} \partial_{\boldsymbol{d}_c} \psi \\ \partial_{\boldsymbol{d}_t} \psi \end{bmatrix} \tag{54}$$

which can be compactly written in an algebraic form as $D (\nabla \psi)_{\mathrm{fc}} = \boldsymbol{w}$. By solving the local face-centered system (54), correction (11b) is finally performed.

4.4 Dynamics of the overlapping zone

During the simulation, the foreground mesh moves and, consequently, the background mesh changes its configuration in the zone of the overlapping as well as in the hole. Let $\Omega_i(t)$ be a background cell in a

Table 1: Convergence analysis for Taylor-Green Vortexes in $(-\pi, \pi)^2$ at final time $T = 1$.

h	L^2-error		convergence rate	
	velocity	pressure	velocity	pressure
1.57e-1	2.7636e-5	2.0345e-3	-	-
1.05e-1	8.4817e-6	9.4667e-4	2.95	1.91
7.85e-2	3.8148e-6	6.9023e-4	2.79	1.11
6.28e-2	2.1021e-6	4.8696e-4	2.68	1.57
5.24e-2	1.3363e-6	3.4589e-4	2.49	1.88

neighborhood of the overlapping. From times t^n to t^{n+1}, it can happen one of the following three scenarios:

1. Cell $\Omega_i(t)$ is present at time t^n and it disappears at time t^{n+1} because the hole completely covers it;

2. Cell $\Omega_i(t)$ is not present at time t^n but it appears at time t^{n+1} because the hole gets away;

3. The overlapping zone does not drastically change its configuration with respect to cell $\Omega_i(t)$, thus the cell is present at time t^n and it still continues to be present at time t^{n+1}.

The third case is trivial. For the first case, the algorithm is performed on the vanishing cell because of the computation of fluxes needed by the neighbouring cells and at time t^{n+1} the cell (with data) is suppressed. For the second possibility, information at current time t^n is missing and it is necessary for evolving the same information at next time t^{n+1}. By recalling the previously introduced notation, in this case index i belongs to the overlapping background set $\mathcal{O}_b$. Thus, it is possible to associate to it an index $j = a_{bf}(i)$ in the foreground set $\mathcal{O}_f$ such that information stored in Ω_j^n is known. Successively, a $\mathcal{P}_2$-reconstruction evaluated on Ω_i is employed by using the stencil $\mathcal{S}_j$ of Ω_j^n. Since there are several layers of cells composing the overlapping zone, this ensures stencil $\mathcal{S}_j$ to be entirely defined in the foreground partition and, consequently, the reconstructed data do not need information coming from the other partition where possibly there is the new born cell Ω_i, namely where data themselves want to be approximated. Finally, the algorithm is performed as usual.

5 Numerical results

In Section 5.1 the performances of the algorithm with respect to the order of grid convergence is presented. In Sections 5.2 and 5.3 validations of physical data for simulations of *lid driven cavity* and *flows around cylinders*, respectively, compared to the literature are presented.

5.1 Order of convergence

For measuring the order of convergence of the method we computed the L^2-norm of the mismatch between the numerical solutions (both velocity and pressure) and the exact ones ($\boldsymbol{u}_{ex}, p_{ex}$) for the Green-Taylor vortexes at Re = 100 in the computational domain $\Omega = (-\pi, \pi)^2$ at final time $T = 1$. In particular, the foreground mesh originally covers the subdomain $(-0.76, 0.76)^2$; it is composed of cells of the same characteristic dimension h of cells in the background and it rigidly counterclockwise rotates around the origin of axes accordingly to the mesh velocity $\boldsymbol{V} = 1/2[-y, x]^T$. At the boundaries, the numerical velocity is imposed to be equal to the exact solution. In order to measure the space-time order of convergence, the time step Δt is chosen by respecting the CFL condition; in particular, since at the boundaries the maximum velocity is 1, we set $\Delta t = \mathrm{CFL}\, h/u_\infty$, with CFL = 0.4 and $u_\infty = 1$. Despite the overset configuration is changing due to the rotation of the foreground mesh, the convergence rate for the velocity and the pressure is around 2.50 for the velocity and slightly smaller than 2 for the pressure, as showed in Table 1.

Table 2: Comparison on the primary vortex for the lid driven cavity: maximum stream-function $\Psi_{\max}$, vorticity ω and location of the topological point. The reference into brackets indicates the used methodology.

	$\Psi_{\max}$	ω	x	y
Present	0.1171	1.9721	0.4687	0.5625
Bruneau [33]	0.1179	2.0508	0.4687	0.5625
Bruneau [33] (Upwind)	0.1180	2.0549	0.4687	0.5625
Bruneau [33] (Kawamura [34])	0.1179	2.0557	0.4687	0.5625
Bruneau [33] (Quickest [35])	0.1150	1.9910	0.4687	0.5625
Ghia [36]	0.1179	2.0497	0.4687	0.5625

5.2 The lid driven cavity

In this section we study a lid driven cavity flow at Re = 1000. At the initial time the fluid has zero velocity inside the cavity $\Omega = (0,1)^2$. No shift conditions (i.e., $\boldsymbol{u} \equiv \boldsymbol{0}$) are strongly imposed on all sides of the cavity with exception to the upper boundary where velocity is constant and equal to $[-1,0]^T$. A steady foreground mesh occupies the subdomain $(0.21, 0.79)^2$. Both the background and the foreground meshes are uniform and Cartesian, with a characteristic length $h = 1/128$. Moreover the overlapping configuration is no-shift. We are interested in the steady solution. This solution is reached when the L^2-norm of the difference between the solutions at two consecutive times t^n and t^{n+1} is less than 10^{-10}. Figure 7 shows the streamlines at the steady state. The solution presents a main vortex and two minor vortexes located towards the lower corners of the cavity. The main vortex originates from the upper boundary and moves to the region discretized by the foreground mesh. In order to quantitatively measure this movement, we consider the geometrical topological point where the stream-function Ψ is maximized. Before the steady condition, this topological point moves from the background to the foreground by passing through the overlapping zone. Table 2 resumes the comparison of the maximum stream-function $\Psi_{\max}$ and its location. Along the topological point, also the value of the vorticity ω is reported. All data from the literature for the comparison consider a discretization grid of 128×128. The validation confirms that the presence of the foreground mesh does not influence the performance of the simulation. The results are in good agreements with reference ones. No perturbations to the numerical solution are induced by the foreground mesh in the case of no-shift overlapping condition.

5.3 The cylinders

In this section the method is validated by studying the flow around a cylinder that can be steady or moving. Let $\boldsymbol{u}_\infty$ be the fluid velocity at the inlet boundary of the computational domain. Moreover we recall that $\boldsymbol{u}_B$ is the body velocity (i.e. of the cylinder). Let the dimensionless stress tensor $\mathbb{T}(\boldsymbol{u}, p)$ be defined as

$$\mathbb{T}(\boldsymbol{u}, p) = -pI + \frac{1}{\text{Re}}(\nabla \boldsymbol{u} + \nabla \boldsymbol{u}^T), \tag{55}$$

with I the identity tensor. The fluid dynamics force $\boldsymbol{F}_f$ and torque M_f exerted by the fluid on the cylinder are

$$\boldsymbol{F}_f = \oint_{\partial \Omega_B} \mathbb{T}(\boldsymbol{u}, p) \boldsymbol{n}_B \, \mathrm{d}\gamma_B, \tag{56a}$$

$$M_f = \oint_{\partial \Omega_B} \boldsymbol{r}_B \wedge \mathbb{T}(\boldsymbol{u}, p) \boldsymbol{n}_B \, \mathrm{d}\gamma_B, \tag{56b}$$

where $\boldsymbol{n}_B$ is the unit outer normal to the cylinder and $\boldsymbol{r}_B$ is the position of any point along the boundary $\partial \Omega_B$ of the cylinder. We define the aerodynamics coefficients as $\boldsymbol{C} = 2\boldsymbol{F}_f / (\rho u_\infty^2 D)$, with D the diameter of the cylinder. Finally, let the drag C_D and lift C_L coefficients be $C_D = \boldsymbol{C} \cdot \boldsymbol{e}_x$ and $C_L = \boldsymbol{C} \cdot \boldsymbol{e}_y$, respectively, with $\{\boldsymbol{e}_x, \boldsymbol{e}_y\}$ the canonical basis for $\mathbb{R}^2$.

The geometrical setting in this section is the same for all test cases. For this reason we study the grid convergence on one case and we consider the same set of back- and foreground meshes for all the other
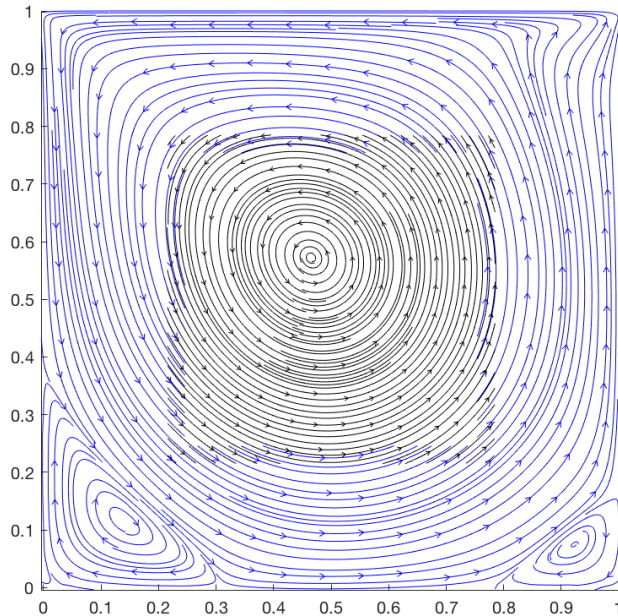
Figure 7: Steady streamlines for the lid driven cavity test: blue for the background and black for the foreground.

Table 3: Features of the five considered Chimera meshes for the convergence grid study. The number of cells in background and foreground are N_b and N_f, respectively, whose sum is N. Label N_B refers to the number of cells around the cylinder.

	Background		Foreground				N
	h	N_b	$\min(h)$	$\max(h)$	N_f	N_B	
Grid1	4.00e-1	2604	2.14e-2	4.00e-1	2686	80	5290
Grid2	3.00e-1	4510	1.11e-2	3.00e-1	4554	100	9044
Grid3	3.00e-1	4510	7.90e-3	3.00e-1	7848	110	12358
Grid4	2.00e-1	10004	7.90e-3	2.00e-1	7194	110	17198
Grid5	1.00e-1	39204	6.90e-3	1.00e-1	18183	210	57387

test cases. This zero test case simulates the flow around a steady cylinder at Re = 550 with an inlet fluid velocity $\boldsymbol{u}_\infty = [1,0]^T$. The center of the cylinder is located in the origin of the axis and is $8D$ far from the inlet boundary, $16D$ from the outlet boundary and $8D$ from any of the upper and lower boundary of the channel. At the boundaries, at the inlet a constant velocity $\boldsymbol{u}_\infty$ is imposed, there are no-reflecting conditions at the outlet [37] and streamline conditions (i.e., $v = 0$ and $\partial_y u = 0$) on the other two boundaries. Since the analytical solution for this case is not available, we compute the drag coefficient evolution in the time window $[0,5]$ for five different Chimera grid configurations, resumed in Table 3. *Grid1* is the coarsest grid and *Grid5* is the finest one. In particular, *Grid3* is an intermediate configuration between *Grid2* and *Grid4*. In fact it mixes the background characteristics of *Grid2* with the foreground ones of *Grid4*. The drag coefficients from the different overset configurations are also compared with the one by Ploumhans and Winckelmans [38] for the same test case. Figure 8 shows the comparison. All curves match the one from the literature and, from the second to the last configuration, the drag coefficient is the same. For this reason we use the Chimera mesh *Grid3* (in Figure 9) because, among all the meshes, it allows a good compromise between computational times and numerical results.
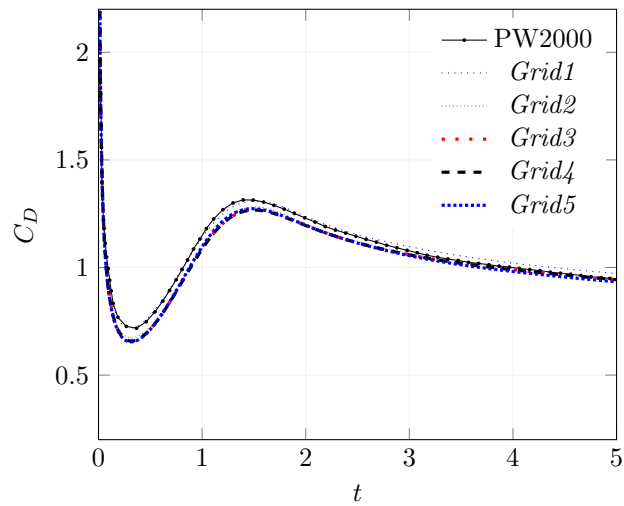
Figure 8: Drag coefficient for the zero test case (steady cylinder at Re = 550). The comparison is also validated with the drag coefficient from Ploumhans and Winckelmans (PW2000) [38].
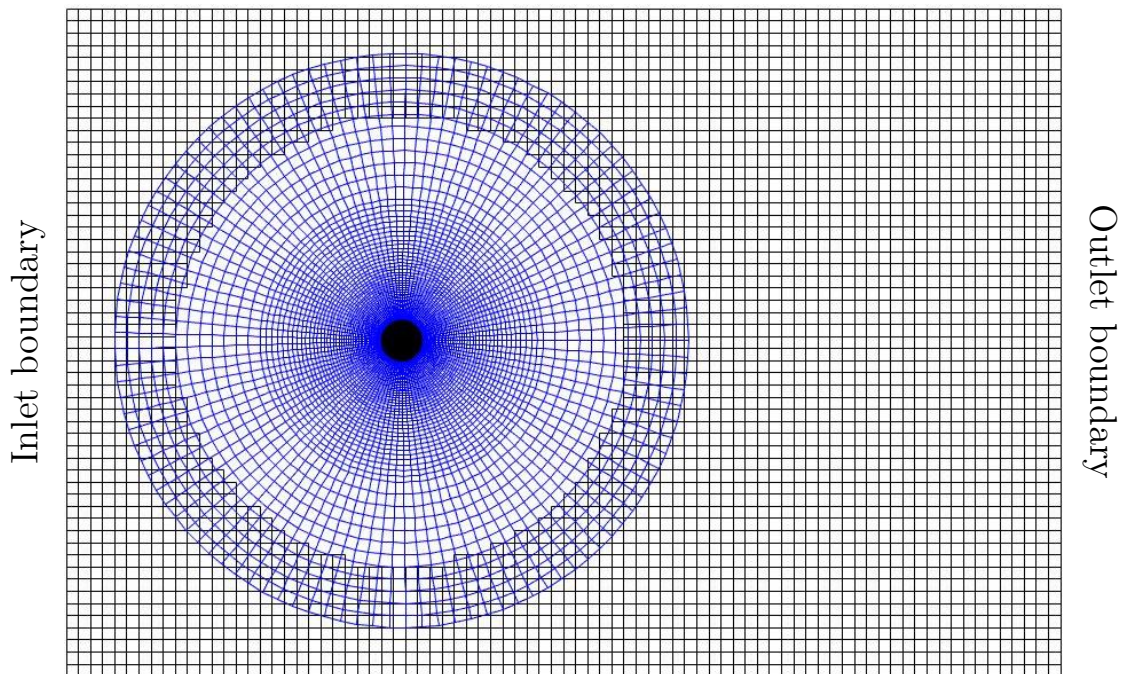

Figure 9: Chimera configuration of *Grid3*.

Table 4: Comparison for the average drag coefficient C_D and the Strouhal number S_t for the steady cylinder at Re = 200.

	C_D	S_t
Present	1.3430	0.1979
Bergmann [39]	1.3900	0.1999
Bergmann Iollo [40]	1.3500	0.1980
Bergmann *et al.* [41]	1.4000	-
Braza *et al.* [42]	1.4000	0.2000
He *et al.* [43]	1.3560	0.1978
Henderson [44]	1.3412	0.1971
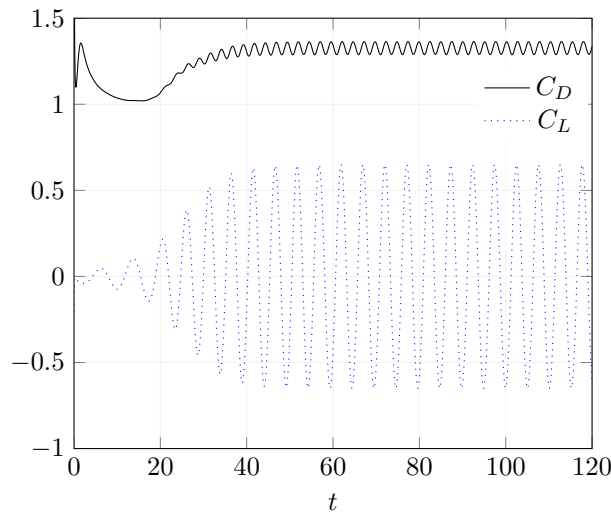
Figure 10: Drag and lift coefficients for the steady cylinder at Re = 200.

5.3.1 Steady cylinder

Let us consider the same configuration of the zero test case for a Reynolds number Re = 200. In particular we study the asymptotic regime (long time integration). For this test case the validation with literature is performed for the average drag coefficient and the Strouhal number $S_t = f_v D / u_\infty$, with f_v the frequency of vortex shedding. The comparison in Table 4 shows that the results obtained with the presented scheme match the results of the literature. In Figure 10 there are the plots of the drag and lift coefficients for the whole time period of integration.

5.3.2 Impulsively started cylinders

We now consider the impulsively started cylinders, namely test cases for which $\boldsymbol{u}_B \neq \boldsymbol{0}$ and $\boldsymbol{u}_\infty = \boldsymbol{0}$. In this case no reflecting conditions are imposed also on the inlet boundary. At the initial time the cylinder is horizontally shifted of $5D$ towards the outlet boundary with respect to the steady test cases. For the whole time interval of integration a constant velocity $\boldsymbol{u}_\infty = [-1,0]^T$ is imposed to the cylinder.

In these conditions, at Re = 550 we expect a similar situation with the zero test case. Thus we compute the drag coefficient by comparing it to both the one of the steady case and the one from the literature provided by Ploumhans and Winckelmans [38] as previously done. The comparison is plotted in Figure 11. The curves for the steady and moving cases are very similar and comparable with the reference literature data. The similarity of the two test cases is also evident from the color plots of the pressure at the same time $t = 5$ in Figure 12.

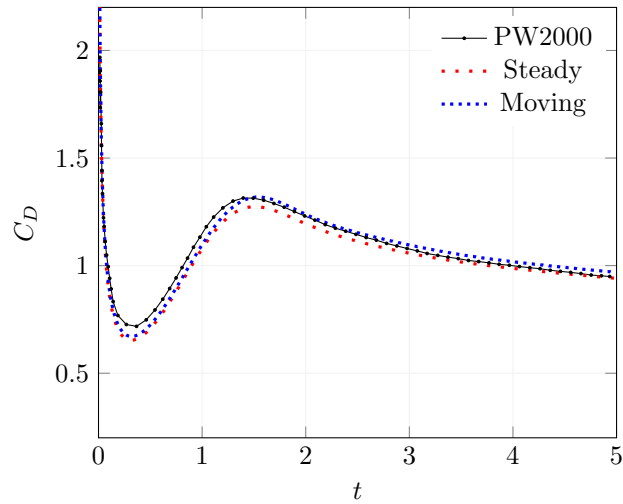As for the steady test cases, we also considered the impulsively started cylinder at Re = 200. By analysing

Figure 11: Comparison of drag coefficient between the steady and impulsively started cylinder at Re = 550. Both are compared with the results by Ploumhans and Winckelmans (PW2000) [38].

the comparison in Figure 13 of the drag coefficient and data from the literature by Koumoutsakos and Leonard (KL1995) [45] and Bergmann *et al.* (BHI2014) [41], there is a good agreement with the previous studies.

5.3.3   Impulsively started then stopped cylinders

With the same boundary conditions of the previous subsection, we also consider test cases where the cylinder is impulsively starting its movement and at a given time t_0 it stops. For this subsection we consider a viscous-dominant flow at Re = 40 and a convective-dominant flow at Re = 550. For the former case the stopping time $t_0 = 5$, while in the latter case the cylinder is stopped at $t_0 = 2.5$. For both cases, before stopping, the cylinder has a constant velocity $\boldsymbol{u}_B = [-1, 0]^T$. Figures 14 and 15 show the plot of the evolution of the drag coefficient compared with data from literature provided by Koumoutsakos and Leonard [45] and Bergmann *et al.* [41] for both test cases. Also in this case present data match the previous studies.

With the same accuracy, evaluated against the test cases of Bergmann *et al.* [41], the validated data though the presented method require the mesh to be composed of a number of cells from 1 to 2 orders of magnitude less. As a matter of fact, if the degrees of freedom in [41] and [40] are $\sim 10^6$ and $\sim 10^5$, respectively, the overset grid exploits $\sim 10^4$ spatial cells.

6   Sedimentation of a cylinder

The last test case analyses the sedimentation of a cylinder in a cavity. In order to validate the computed data with the proposed method, we set the same configuration by Coquerelle and Cottet [46], Bergmann *et al.* [41] and Bergmann and Iollo [40]. The cavity is defined by the vertical channel $[0, 2] \times [0, 6]$ with a two-dimensional cylinder, with its center of mass originally located in $(1, 4)$, falls subjected to the gravity up to the lower boundary. The cylinder radius is $r = 0.125$ with a density $\rho_s = 1.5$. The viscosity and the density of the bounding fluid are $\nu = 0.01$ and $\rho_f = 1.0$, respectively. The gravity has a modulus $g = -980$. The cylinder moves accordingly to

$$\boldsymbol{u}_B = \boldsymbol{V} + \boldsymbol{\Omega} \wedge (\boldsymbol{x} - \boldsymbol{x}_G), \tag{57a}$$

$$m_B \dot{\boldsymbol{V}} = -\boldsymbol{F}_f + \tilde{m} \boldsymbol{g}, \tag{57b}$$

$$J_B \dot{\boldsymbol{\Omega}} = M_f, \tag{57c}$$
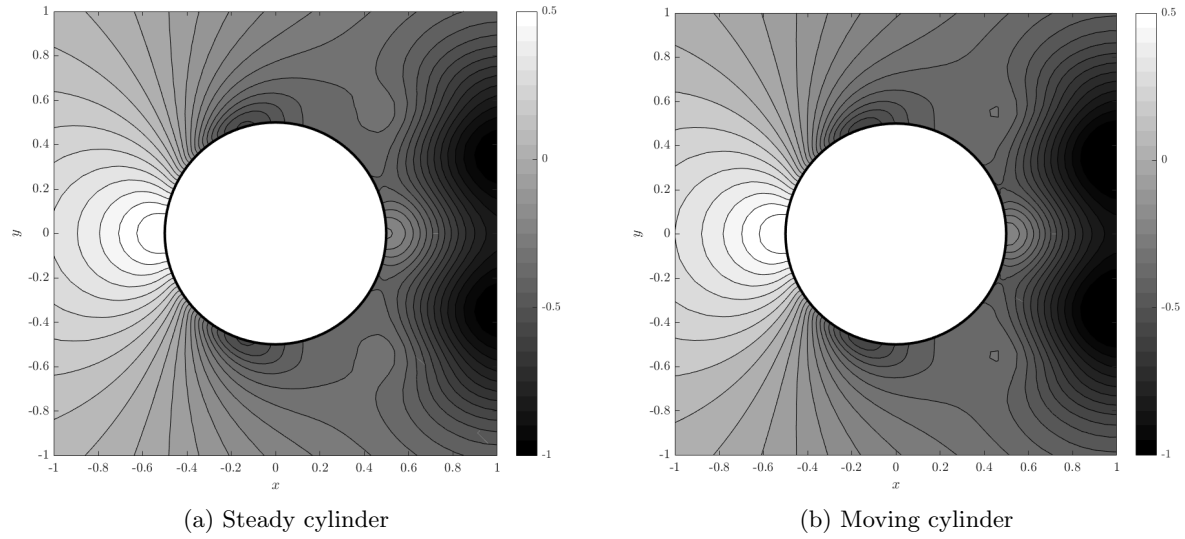
(a) Steady cylinder

(b) Moving cylinder

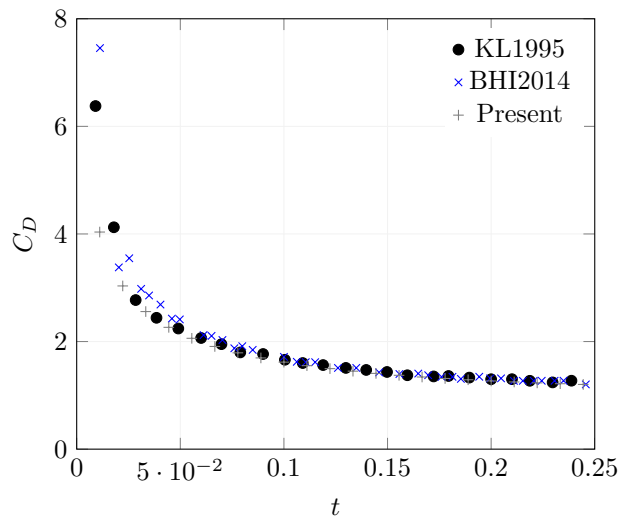Figure 12: Pressure at $t = 5$ for steady and impulsively moving cylinders at Re $= 550$.

Figure 13: Comparison of the evolution of the drag coefficient up to $t = 0.25$ for the impulsively started cylinder at Re $= 200$ with data by Koumoutsakos and Leonard (KL1995) [45] and Bergmann *et al.* (BHI2014) [41].
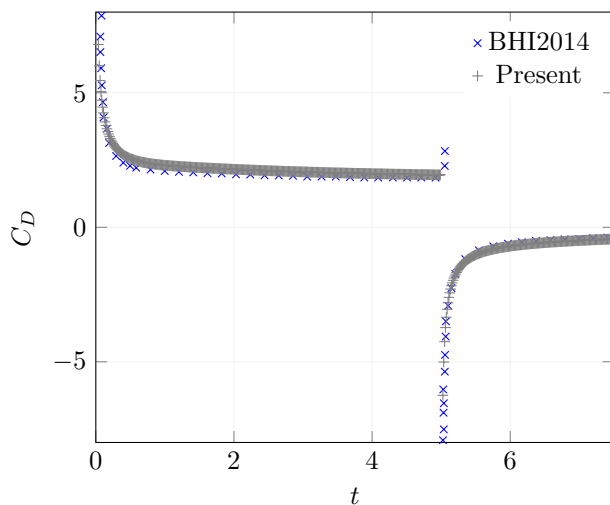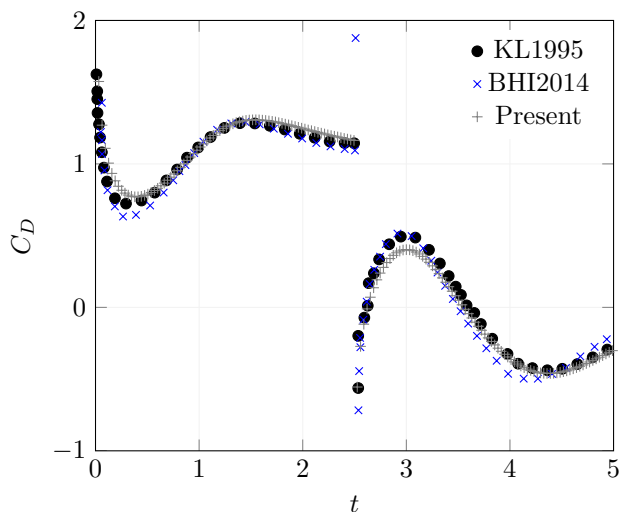
Figure 14: Comparison of the evolution of the drag coefficient up to $t = 7.5$ for the impulsively started and then stopped cylinder at Re $= 40$ with data by Bergmann *et al.* (BHI2014) [41].

Figure 15: Comparison of the evolution of the drag coefficient up to $t = 5$ for the impulsively started and then stopped cylinder at Re $= 550$ with data by Koumoutsakos and Leonard (KL1995) [45] and Bergmann *et al.* (BHI2014) [41].

where $\boldsymbol{V}$ and $\boldsymbol{\Omega}$ are the translation and rotational velocities, respectively, and $\boldsymbol{x}_G$ is the center of the cylinder; in the translation equation (57b) $m_B = \pi r^2 \rho_s$ is the cylinder mass while $\tilde{m} = \pi r^2 (\rho_s - \rho_f)$ is the difference of fluid and cylinder masses after the Archimedes' law; in the rotational equation (57c) the cylinder inertia is denoted by $J_B = \pi r^4 \rho_s$; finally $\boldsymbol{F}_f$ and M_f are the fluid dynamics forces and torque defined in (56), respectively.

The background mesh is uniform and Cartesian with cells of size $h = 5 \times 10^{-2}$. The foreground mesh fits the cylinder shape with the characteristic lengths of the cell varying from 1.4×10^{-3} to 5×10^{-2}. The time step is $\Delta t = \min(h)/20$. Since we are interested in simulating the cylinder up to the lower boundary, there exists a time t_0 after which the foreground mesh overcomes the physical boundaries of the cavity, as showed in Figure 16. In order to manage the part of the foreground mesh exceeding the physical domain, we extend the computational domain as $\tilde{\Omega} = (0, 2) \times (-1, 2)$ such that the foreground mesh is always fully contained. Thus, the exceeding region is discretized by a part of the background and, and for any time $t > t_0$, by a part of the foreground mesh. Consequently, also the hole in the background will overcome the physical boundary after t_0. In the whole computational domain a fluid-solid single flow is considered by modeling a solid material in the extended part (i.e., for any $y < 0$). This single flow is computed via a penalization method [5]. With this approach the entire system is considered as a porous medium with a variable discontinuous permeability K. In particular, the extended domain simulates an impermeable body with a very low permeability (i.e., $K \ll 1$). In this case, the considered equation in place of (2) reads

$$\frac{\partial \boldsymbol{u}}{\partial t} + \nabla \cdot (\boldsymbol{u} \boldsymbol{u}^T) = -\nabla p + \frac{1}{\mathrm{Re}} \Delta \boldsymbol{u} + \frac{\chi_W}{K} (\boldsymbol{u}_W - \boldsymbol{u}), \tag{58}$$

where $\boldsymbol{u}_W$ is the velocity of the wall, zero in our case, and χ_W is the characteristic function defined as

$$\chi_W = \begin{cases} 1, & \text{in the wall} \\ 0, & \text{elsewhere} \end{cases}. \tag{59}$$

In the limit of $K \to 0$, equation (58) tends to the Navier-Stokes equation (2) [5]. In this test case $K = 10^{-8}$. Despite in principle the penalization method can be used also for the cylinder, we remark that in this case we use is only for managing the extended part of the computational domain. In particular, we consider the solid below the wall having the same density of the cylinder (i.e., $\rho_s = 1.5$). Since the new reaction term in (58) affects the velocity, with respect to the fractional Chorin-Temam method, it is included in the predictor solution (7). Thus, it implies the ADER scheme to consider a reaction no-stiff source term [29]. In particular, in the local space-time Galerkin solution for equation (20), a pseudo-mass term arises as

$$\frac{\Delta t}{K} \langle \theta_m, \chi_W |_{\hat{\boldsymbol{\xi}}_l} \theta_l \rangle \hat{q}_{k,l} \tag{60}$$

for $m, l = 1, \ldots, 27$, with $\chi_W |_{\hat{\boldsymbol{\xi}}_l} = \chi_W(x(\hat{\boldsymbol{\xi}}_l), y(\hat{\boldsymbol{\xi}}_l))$ is the characteristic function composed with the spatial components of the reference map $\mathcal{M}_i$ along the l-th tensor Gauss-Legendre quadrature point. Successively, for the fixed-point problem (21), at the iteration r, this reaction term (60) yields an unknown component as $\Delta t / K \langle \theta_m, \chi_W |_{\hat{\boldsymbol{\xi}}_l} \theta_l \rangle \hat{q}_{k,l}^{r+1}$. During the ADER correction step (27), the penalization term is just added at the left hand side of the space-time divergence form as

$$\nabla_{\boldsymbol{x},t} \cdot \boldsymbol{\mathcal{U}}_{\boldsymbol{k}} + \frac{\chi_W}{K} u_k = 0. \tag{61}$$

In order to write the FV scheme, by integrating the above expression in the physical space-time slab $\mathcal{C}_i^n$, the method becomes

$$-|\Omega_i^n| \bar{u}_{k,i}^{*,n} + |\Omega_i^{n+1}| \bar{u}_{k,i}^{*,n+1} + \sum_{j=1}^{4} \iint_{\Gamma_{ij}^n} \boldsymbol{\mathcal{U}}_k \cdot \boldsymbol{n}_{\boldsymbol{x},t} \, \mathrm{d}\Gamma + \iiint_{\mathcal{C}_i^n} \frac{\chi_W}{K} u_k \, \mathrm{d}\mathcal{C} = 0. \tag{62}$$

Scheme (62) is not affected in the space-time fluxes by the new reaction term. For this reason, the procedure of the method remains the same as explained in Section 4.1.
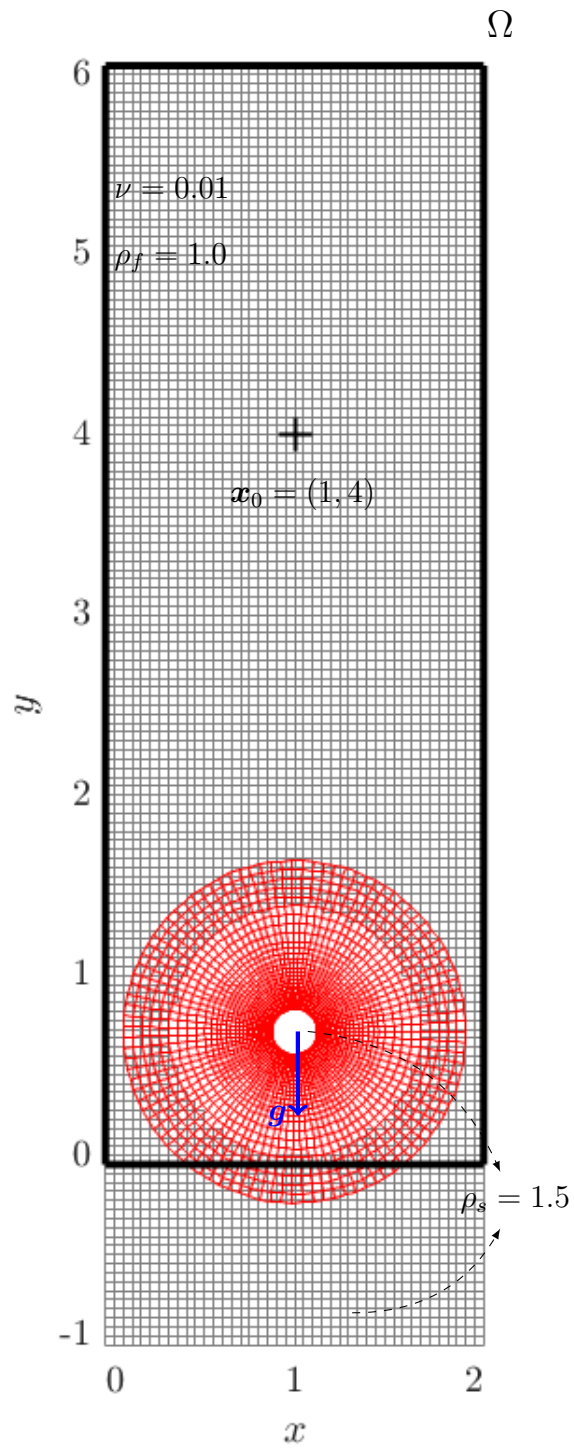
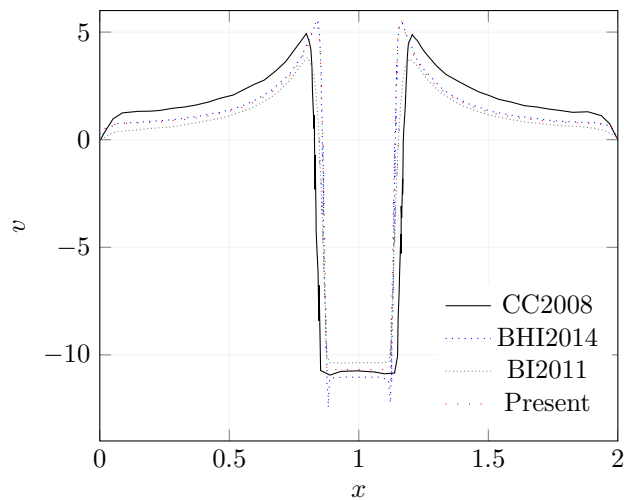Figure 16: Chimera configuration for the sedimentation cylinder.

Figure 17: Comparison of the vertical velocity v on a horizontal cut through the center of the cylinder at time $t = 0.1$ for the sedimentation test case with data by Coquerelle and Cottet (CC2008) [46], Bergmann *et al.* (BHI2014) [41] and Bergmann and Iollo (BI2011) [40].
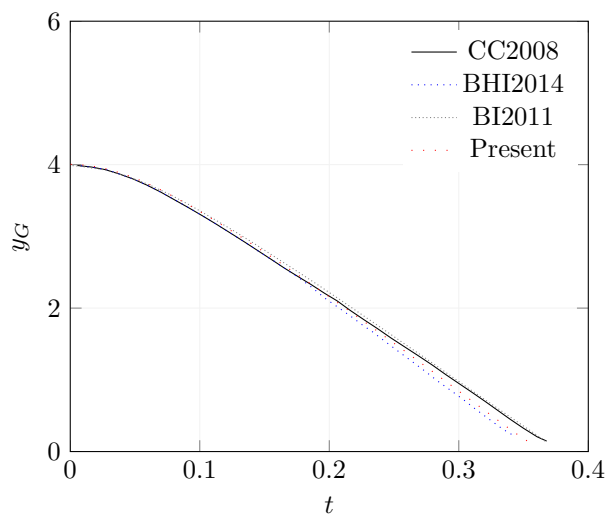

Figure 18: Comparison of the evolution of the vertical position y_G of the center of the cylinder for the sedimentation test case with data by Coquerelle and Cottet (CC2008) [46], Bergmann *et al.* (BHI2014) [41] and Bergmann and Iollo (BI2011) [40].

Figures 17 and 18 show the validation for the vertical velocity on the horizontal line cutting the cylinder along the center and the evolution of the heigth of the cylinder, respectively. Present data present good agreement with all the ones from the literature. In particular it is possible to remark a closer match with the curves by Bergmann *et al.* [41]; indeed both the present method and the method used in that paper are second-order accurate. Also in this case it is possible to remark the sensible decreasing of degrees of freedom needed by the numerical solution through the presented method with respect to the ones from the literature. In fact if the overset grid is composed of 9267 cells (i.e., 5964 in the background and 3663 in the foreground), grids employed in [46], [41] and [40] use about 3×10^6, 8×10^5 and 2×10^6 cells.

7 Conclusions

We presented a FV scheme that is second-order accurate in space and time for the solution of the incompressible Navier-Stokes equations with moving meshes. The method is based on the Chorin-Temam fractional step method. The predictor velocity is solved through an extension of the ADER method for a nonlinear convective-diffusive system on a Chimera mesh with a compact data transmission condition for fringe cells, i.e., those cells devoted to the communication between the different meshes of the overset grid. The projection step exploits a FV hybrid method for the reconstruction of the pressure gradient. In particular a geometric approach is used for internal cells and a weighted expansion is employed for expressing the gradient along the fringe cells. We proved that the approaches for internal and fringe cells are the same in the limit of a no-shif overlapping condition. This result is achieved by properly minimizing a convex function for the local coefficients allowing to take into account both the second-order truncation of the solution and the distribution of data in the local stencil.

The numerical results showed that the movement of the mesh does not introduce sporious oscillation to the numerical solution of the problem and that second-order accuracy is preserved in both space and time. In order to test the method, a wide range of canonical cases is exposed. Their validation confirms that the obtained data match the ones from the literature. In particular, results for tests where the exact solution is not available are always closer to the ones obtained by second-order methods. Moreover, at equal accuracy, the total number of cells for the overset grid (namely the degrees of freedom) is reduced by up to two orders of magnitude compared to the ones from the cited literature. With the sedimentation test case, we introduced a reaction term which is not present *a priori* in the original equation. In particular, we mixed the adapted ADER method for Chimera meshes with a penalization method in order not to cut part of the foreground mesh that overcomes the physical boundaries of the domain. This application highlights the versatility of the proposed method even in proximity of boundaries defined on other mesh blocks. Extension to three-dimensional flows on octree meshes is now envisaged.

Acknowledgements

References

[1] C. W. Hirt, A. A. Amsden, J. Cook, An arbitrary lagrangian-eulerian computing method for all flow speeds, Journal of computational physics 14 (3) (1974) 227–253.

[2] F. Duarte, R. Gormaz, S. Natesan, Arbitrary lagrangian–eulerian method for navier–stokes equations with moving boundaries, Computer Methods in Applied Mechanics and Engineering 193 (45-47) (2004) 4819–4836.

[3] F. Gibou, R. P. Fedkiw, L.-T. Cheng, M. Kang, A second-order-accurate symmetric discretization of the poisson equation on irregular domains, Journal of Computational Physics 176 (1) (2002) 205–227.

[4] R. Mittal, G. Iaccarino, Immersed boundary methods, Annu. Rev. Fluid Mech. 37 (2005) 239–261.

[5] P. Angot, C.-H. Bruneau, P. Fabrie, A penalization method to take into account obstacles in incompressible viscous flows, Numerische Mathematik 81 (4) (1999) 497–520.

[6] R. Glowinski, T.-W. Pan, J. Periaux, A fictitious domain method for dirichlet problem and applications, Computer Methods in Applied Mechanics and Engineering 111 (3-4) (1994) 283–303.

[7] C. S. Peskin, The immersed boundary method, Acta numerica 11 (2002) 479–517.

[8] R. Abgrall, H. Beaugendre, C. Dobrzynski, An immersed boundary method using unstructured anisotropic mesh adaptation combined with level-sets and penalization techniques, Journal of Computational Physics 257 (2014) 83–101.

[9] E. Volkov, The method of composite meshes for finite and infinite regions, Automatic Programming, Numerical Methods and Functional Analysis 96 (96) (1970) 145.

[10] J. Benek, P. Buning, J. Steger, A 3-d chimera grid embedding technique, in: 7th Computational Physics Conference, 1985, p. 1523.

[11] R. Meakin, Chapter 11: Composite overset structured grids, Handbook of grid generation, JF Thompson, BK Soni and NP Weatherill. CRC.

[12] N. A. Petersson, Hole-cutting for three-dimensional overlapping grids, SIAM Journal on Scientific Computing 21 (2) (1999) 646–665.

[13] J. Guerrero, Overset composite grids for the simulation of complex moving geometries, DICAT, University of Genoa, Italy.

[14] Z. Wang, A fully conservative interface algorithm for overlapped grids, Journal of Computational Physics 122 (1) (1995) 96–106.

[15] M.-S. Liou, Y. Zheng, A novel approach of three-dimensional hybrid grid methodology: Part 2. flow solution, Computer methods in applied mechanics and engineering 192 (37-38) (2003) 4173–4193.

[16] I.-T. Chiu, R. Meakin, On automating domain connectivity for overset grids, in: 33rd Aerospace Sciences Meeting and Exhibit, 1995, p. 854.

[17] G. Houzeaux, J. Cajas, M. Discacciati, B. Eguzkitza, A. Gargallo-Peiró, M. Rivero, M. Vázquez, Domain decomposition methods for domain composition purpose: Chimera, overset, gluing and sliding mesh methods, Archives of Computational Methods in Engineering 24 (4) (2017) 1033–1070.

[18] A. J. Chorin, Numerical solution of the navier-stokes equations, Mathematics of computation 22 (104) (1968) 745–762.

[19] R. Temam, Sur l'approximation de la solution des équations de navier-stokes par la méthode des pas fractionnaires (ii), Archive for rational mechanics and analysis 33 (5) (1969) 377–385.

[20] M. Dumbser, W. Boscheri, M. Semplice, G. Russo, Central weighted eno schemes for hyperbolic conservation laws on fixed and moving unstructured meshes, SIAM Journal on Scientific Computing 39 (6) (2017) A2564–A2591.

[21] V. A. Titarev, E. F. Toro, Ader schemes for three-dimensional non-linear hyperbolic systems, Journal of Computational Physics 204 (2) (2005) 715–736.

[22] V. A. Titarev, E. F. Toro, Ader: Arbitrary high order godunov approach, Journal of Scientific Computing 17 (1) (2002) 609–618.

[23] C. E. Castro, E. F. Toro, Solvers for the high-order riemann problem for hyperbolic balance laws, Journal of Computational Physics 227 (4) (2008) 2481–2513.

[24] M. Bergmann, M. G. Carlino, A. Iollo, Second order scheme for unsteady advection-diffusion on moving overset grids with a compact transmission condition, hal-03119830.

[25] E. Bertolazzi, G. Manzini, A cell-centered second-order accurate finite volume method for convection–diffusion problems on unstructured meshes, Mathematical Models and Methods in Applied Sciences 14 (08) (2004) 1235–1260.

[26] Y. Coudière, J.-P. Vila, P. Villedieu, Convergence rate of a finite volume scheme for a two dimensional convection-diffusion problem, ESAIM: Mathematical Modelling and Numerical Analysis 33 (3) (1999) 493–516.

[27] A. Raeli, M. Bergmann, A. Iollo, A finite-difference method for the variable coefficient poisson equation on hierarchical cartesian meshes, Journal of computational physics 355 (2018) 59–77.

[28] R. Mittal, H. Dong, M. Bozkurttas, F. Najjar, A. Vargas, A. Von Loebbecke, A versatile sharp interface immersed boundary method for incompressible flows with complex boundaries, Journal of computational physics 227 (10) (2008) 4825–4852.

[29] A. Hidalgo, M. Dumbser, Ader schemes for nonlinear systems of stiff advection–diffusion–reaction equations, Journal of Scientific Computing 48 (1) (2011) 173–189.

[30] W. Boscheri, M. Dumbser, Arbitrary-lagrangian-eulerian one-step weno finite volume schemes on unstructured triangular meshes, Communications in Computational Physics 14 (5) (2013) 1174–1206.

[31] G. B. Nagy, O. E. Ortiz, O. A. Reula, The behavior of hyperbolic heat equations' solutions near their parabolic limits, Journal of Mathematical Physics 35 (8) (1994) 4334–4356.

[32] E. F. Toro, G. I. Montecinos, Advection-diffusion-reaction equations: hyperbolization and high-order ader discretizations, SIAM Journal on Scientific Computing 36 (5) (2014) A2423–A2457.

[33] C.-H. Bruneau, M. Saad, The 2d lid-driven cavity problem revisited, Computers & fluids 35 (3) (2006) 326–348.

[34] T. Kawamura, H. Takami, K. Kuwahara, New higher-order upwind scheme for incompressible navier-stokes equations, in: Ninth International Conference on Numerical Methods in Fluid Dynamics, Springer, 1985, pp. 291–295.

[35] B. Leonard, The ultimate conservative difference scheme applied to unsteady one-dimensional advection, Computer methods in applied mechanics and engineering 88 (1) (1991) 17–74.

[36] U. Ghia, K. N. Ghia, C. Shin, High-re solutions for incompressible flow using the navier-stokes equations and a multigrid method, Journal of computational physics 48 (3) (1982) 387–411.

[37] G. Jin, M. Braza, A nonreflecting outlet boundary condition for incompressible unsteady navier-stokes calculations, Journal of computational physics 107 (2) (1993) 239–253.

[38] P. Ploumhans, G. Winckelmans, Vortex methods for high-resolution simulations of viscous flow past bluff bodies of general geometry, Journal of Computational Physics 165 (2) (2000) 354–406.

[39] M. Bergmann, Optimisation aérodynamique par réduction de modele pod et contrôle optimal. application au sillage laminaire d'un cylindre circulaire, Institut National Polytechnique de Lorraine.

[40] M. Bergmann, A. Iollo, Modeling and simulation of fish-like swimming, Journal of Computational Physics 230 (2) (2011) 329–348.

[41] M. Bergmann, J. Hovnanian, A. Iollo, An accurate cartesian method for incompressible flows with moving boundaries, Communications in Computational Physics 15 (5) (2014) 1266–1290.

[42] M. Braza, P. Chassaing, H. H. Minh, Numerical study and physical analysis of the pressure and velocity fields in the near wake of a circular cylinder, Journal of fluid mechanics 165 (1986) 79–130.

[43] J.-W. He, R. Glowinski, R. Metcalfe, A. Nordlander, J. Periaux, Active control and drag optimization for flow past a circular cylinder: I. oscillatory cylinder rotation, Journal of Computational Physics 163 (1) (2000) 83–117.

[44] R. D. Henderson, Details of the drag curve near the onset of vortex shedding, Physics of Fluids 7 (9) (1995) 2102–2104.

[45] P. Koumoutsakos, A. Leonard, High-resolution simulations of the flow around an impulsively started cylinder using vortex methods, Journal of Fluid Mechanics 296 (1995) 1–38.

[46] M. Coquerelle, G.-H. Cottet, A vortex level set method for the two-way coupling of an incompressible fluid with colliding rigid bodies, Journal of Computational Physics 227 (21) (2008) 9121–9137.